



## Article

# Impact of the Structural Parameters on the Performance of a Regenerative-Type Hydrogen Recirculation Blower for Vehicular Proton Exchange Membrane Fuel Cells

Xu Liang <sup>1</sup> , Huifang Kang <sup>1,\*</sup> , Rui Zeng <sup>1</sup>, Yue Pang <sup>1</sup>, Yun Yang <sup>2</sup>, Yunlu Qiu <sup>2</sup>, Yuanxu Tao <sup>2</sup> and Jun Shen <sup>1</sup>

<sup>1</sup> School of Mechanical Engineering, Beijing Institute of Technology, Beijing 100081, China

<sup>2</sup> Shandong Kaigrisen Energy Technology Co., Ltd., Jinan 264006, China; YuanxuT@126.com (Y.T.)

\* Correspondence: kanghf@bit.edu.cn; Tel.: +86-10-68914304

**Abstract:** The compact structure and stable performance of regenerative blowers at small flow rates render them attractive for the development of hydrogen recirculation devices for fuel cells. However, its optimization of structural parameters has not been yet reported in the literature. Along these lines, in this work, a mechanistic study was carried out in terms of examining the role of the flow channel structure on the performance of a regenerative-type hydrogen recirculation blower for the fabrication of automotive fuel cells. A three-dimensional computational fluid dynamics (CFDs) model of the regenerative blower was established, and the accuracy of the proposed model was verified through experimental data. The impact of structural parameter interactions on the performance of the regenerative blower was investigated using CFD technology, response surface methodology (RSM), and genetic algorithm (GA). First, the range of the structural parameters was selected according to the actual operation, and the influence of a single geometric factor on the efficiency was thoroughly investigated using CFD simulation. Then, a second-order regression model was successfully established using RSM. The response surface model was solved using GA to obtain the optimized geometric parameters and the reliability of the GA optimization was verified by performing CFD simulations. From our analysis, it was demonstrated that the interaction of the blade angle and impeller inner diameter has a significant impact on efficiency. The entropy generation analysis showed also that the internal flow loss of the optimized regenerative blower was significantly reduced, and the design point efficiency reached 51.7%, which was significantly improved. Our work provides a novel solution for the design of a recirculation blower and offers a reference for the optimization of regenerative-type hydrogen blowers.

**Keywords:** hydrogen recirculation; regenerative blower; interaction of parameters; response surface methodology; entropy generation



**Citation:** Liang, X.; Kang, H.; Zeng, R.; Pang, Y.; Yang, Y.; Qiu, Y.; Tao, Y.; Shen, J. Impact of the Structural Parameters on the Performance of a Regenerative-Type Hydrogen Recirculation Blower for Vehicular Proton Exchange Membrane Fuel Cells. *Sustainability* **2024**, *16*, 1856. <https://doi.org/10.3390/su16051856>

Academic Editors: Francesco Ferella and Mirco Peron

Received: 21 December 2023

Revised: 23 January 2024

Accepted: 19 February 2024

Published: 23 February 2024



**Copyright:** © 2024 by the authors. Licensee MDPI, Basel, Switzerland. This article is an open access article distributed under the terms and conditions of the Creative Commons Attribution (CC BY) license (<https://creativecommons.org/licenses/by/4.0/>).

## 1. Introduction

The growth rate in the number of automobiles globally has raised concerns about the growing environmental pollution and energy crisis [1]. To this end, in view of the large demand for fossil fuels in conventional internal combustion engine vehicles, as well as the problems of atmospheric pollution and the greenhouse effect [2], some countries have taken action to reduce carbon emissions for realizing global energy sustainability [3]. As a result, there is an urgent need for the exploitation of other alternative sustainable energy sources. A promising alternative to future fossil fuel-based energy systems appears to be hydrogen energy [4]; hydrogen has a high energy density and its oxidation product consists of pure water, which is a sustainable green energy source with abundant reserves [5–7]. Moreover, hydrogen energy is also a widely discussed source of renewable energy with strong links to sustainability; it can be used as a clean energy source, and by using renewable energy sources, such as solar or wind, to generate hydrogen, dependence on conventional energy sources can be reduced. Thereby, hydrogen energy can reduce greenhouse gas emission

to advance sustainability, and as a result, it plays an increasingly important role on the world energy stage [8]. Some scholars have called it “the ultimate energy source of the 21st century” [9].

As one of the main ways to utilize hydrogen energy, proton exchange membrane fuel cells (PEMFCs) are ideally suited for vehicles and are considered a clean energy technology with strong links to sustainability. Due to their high energy density, high efficiency, fast start up, zero emission, and low maintenance and noise, they are viewed as the most promising green energy converters to replace conventional internal combustion engines [5,10,11]. Compared to renewable energy sources such as solar and wind turbines, hydrogen fuel cells are not affected by environmental factors such as temperature, seasons, and geology [12]. Recently, PEMFCs have attracted many companies and institutes to participate in the development of their technology [13].

The core of a hydrogen fuel cell vehicle is the PEMFC [14], where in practice, to avoid the risk of fuel shortage, the anode inlet of the PEMFC always passes into the excess hydrogen [15–17]. Alarming, if the unreacted hydrogen inside the stack is directly discharged from the anode outlet, it will not only reduce the efficiency of the PEMFC, but there is also a safety hazard. To ensure the reliable and high-efficiency operation of the PEMFC and enhance the hydrogen utilization rate, hydrogen recirculation devices are generally used to re-pressurize the anode outlet and send it back to the hydrogen supply line. Then, the gas re-mixed with the fresh hydrogen from the gas cylinder enters the stack to perform an electrochemical reaction; a simplified anodic hydrogen recirculation system is shown in Figure 1. Additionally, during the operation of the hydrogen recirculation device, excess water can be also brought out by recirculating the excess hydrogen, effectively preventing flooding of the stack.

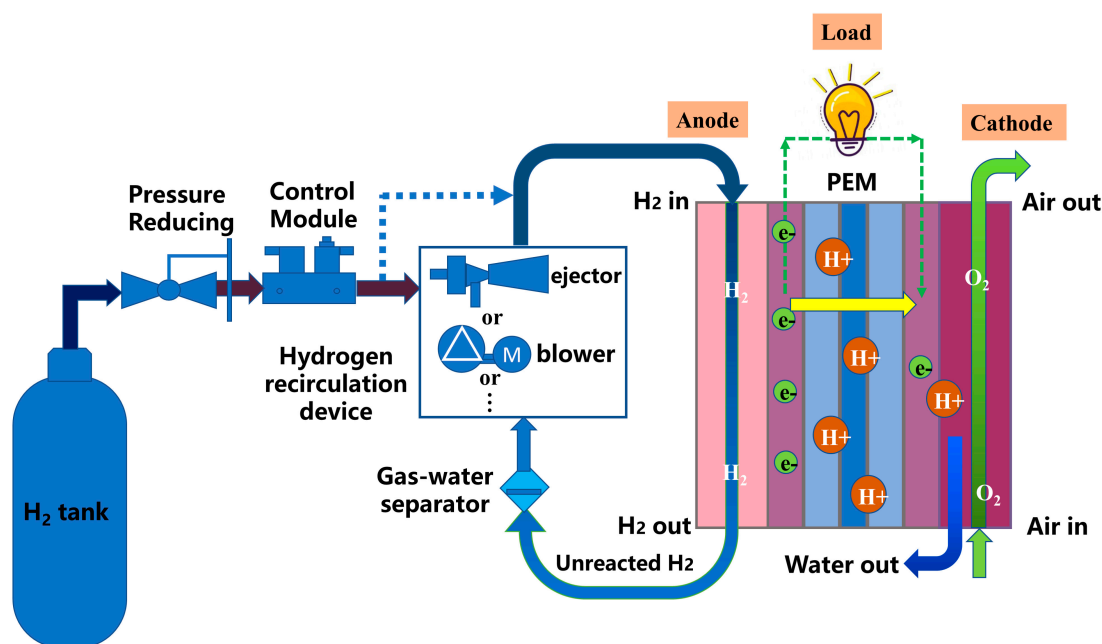


**Figure 1.** Schematic illustration of a simplified anodic hydrogen recirculation system.

Currently, the main hydrogen recirculation devices for automotive fuel cells are ejectors, blowers, and their combinations. Ejectors are characterized by a compact structure, reliable operation, no moving elements, no parasitic power, and no pollution [18]. The high-pressure hydrogen from the vehicle cylinder flows into the ejector as the primary flow, its velocity increases, and the pressure decreases after passing through the nozzle. The unreacted hydrogen and water vapour from the stack anode outlet are called secondary flow, which is sucked into the secondary inflow port under the impact of pressure difference. Subsequently, these two fluids flow into the mixing chamber together, inside the mixing

chamber, where they mix with each other and their velocities are balanced correspondingly. At the mixing chamber outlet, the velocity of the mixed fluid is almost uniform. Then, the mixed fluid flows into the diffuser, and under the impact of diffusion, the static pressure increases and the velocity decreases. The mixed fluid pressure at the outlet of the ejector is higher than the anode exhaust, and the increased pressure of the mixed fluid meets the inlet requirements of the anode of the stack. Finally, the fluid runs into the anode inlet to complete the process of recirculation [14]. The properties of ejectors have been extensively examined in the literature, including their design [19–23] and optimization [1,5,15,24–30]. However, neither single ejectors [31], variable cross-section ejectors [23], multi-nozzle ejectors [32], nor dual-ejector combinations [33] can fully satisfy the entire range of fuel cell operations. On top of that, ejectors are particularly unable to reach a high entrainment ratio in the case of small power operations.

Mechanical blowers driven by motors can also realize hydrogen recirculation, and recirculation blowers are easy to control and have superior performance at non-designed points, which have been broadly used as hydrogen circulation devices, particularly for automotive applications [34]. However, if a recirculation blower is used alone to realize hydrogen recirculation under the whole condition of the cell, the motor will inevitably consume too much extra power of the electric stack. Therefore, future development schemes of hydrogen recirculation devices should include the utilization of the ejector in parallel with a recirculation blower [14], where the ejector can realize hydrogen recirculation under medium- and high-power operation, and the blower operates at the small power point of the electric stack, which will not consume too much electric power.

Currently, the mechanical blowers applied in the hydrogen recirculation field are mainly volumetric and vane-type blowers. In terms of positive displacement blowers, claw blowers are characterized by a simple and compact structure, high reliability, and the ability to run without oil [35]. Hydrogen molecules are particularly small and very easy to leak. Therefore, the claw blower requires a precise fit between its components, which increases its manufacturing cost accordingly. Furthermore, the clearance between the two claws, as well as between the claws and the housing, is particularly narrow, which could also cause severe component wear problems. Meanwhile, with the rising internal pressure during operation, the saturated water vapour in the anode exhaust gas of the stack will cross the saturation line to produce liquid water. Under the action of surface tension, the liquid water will gather in the internal gap of the blower and condense into liquid droplets. Because of the cold weather in the winter in northern areas, the condensed liquid droplets inside the blower will freeze, resulting in the inability of the claw blower to operate, which seriously impedes its use. It is clear from the above-mentioned analysis that the severe wear, short life, and icing problems of claw blowers limit their use in hydrogen recirculation systems. Roots blowers have the characteristics of relatively low compression efficiency and high electricity consumption, and operate without built-in compression [34], while similar to claw blowers, Roots blowers also require a high machined fit of the rotor. In addition, high vibration and noise vibration limit their use in PEMFC vehicles [36]. Additionally, with the increasing power of fuel cells, the required pressure rise of anodes is also increasing; however, the structural limitations of the Roots blower and its low energy efficiency at high discharge pressure ratio conditions [37,38] limit its wide implementation. Compared with the above blowers, scroll blowers have the advantages of small size and light weight [39], but their outlet pressure fluctuates greatly, which adversely affects the proton exchange membrane inside the stacks. Meanwhile, the machining of the scroll compression surface and its inspection are very complex, requiring high-precision manufacturing and precise centring assembly techniques, which increase the manufacturing costs. The sealing between the two scroll disks also increases the wear of the end faces, and if a certain motion gap is maintained, it leads to increased leakage and reduced performance [14]. Diaphragm pumps can operate without oil conditions, and for compressed hydrogen, no leakage can be generated, which can ensure the purity of the gas [40]. Nonetheless, frequent diaphragm failures are a fatal disadvantage of diaphragm blowers [41], and therefore, diaphragm life

must be ensured before being applied to large-scale applications [41,42]. For vane-type blowers, centrifugal blowers have the characteristics of compact structure, highly efficient operation [43], and low noise and wear; these advantages are particularly necessary for vehicles. However, some works in the literature have argued that the centrifugal blower's speed must reach hundreds of thousands of revolutions so that the pressure rise can meet the fuel cell anode recirculation, but such high speeds pose significant challenges for the motor and bearing [44]. In addition, flow instabilities, such as surge and stall, are one of the major drawbacks of centrifugal blowers [45]. As far as the head is concerned, regenerative blowers have good performance and can operate without oil, while their simple and compact structure leads to low manufacturing costs [46], and high operational stability even at small flow rates [47]. Currently, in the field of hydrogen recirculation devices for automotive PEMFCs, regenerative blowers with small fluctuations in outlet pressure are considered to be the most likely alternative to positive displacement blowers [48,49]. However, the only drawback of the regenerative blower is its low operation efficiency, which can be attributed to the internal gas gain energy from the impeller due to multiple collisions inside the blower, resulting in relatively high flow losses and efficiencies usually lower than 45–50% [46].

In summary, volumetric blowers need high-precision machining. Additionally, the different degrees of wear seriously reduce their service life. In particular, for vane-type blowers, the centrifugal blower needs to reach hundreds of thousands of RPM; as a result, such high speed not only causes a great deal of trouble in the selection and design of the motor and bearings, but liquid strike on the impellers will be also aggravated, its operation lifespan will be shortened, and at the same time, stalling and surging also limit its use. The regenerative blower possesses the following comparative advantages: (1) small flow conditions can be realized under stable operation, (2) it does not require high-precision machining nor experience wear and tear similar to the volumetric blower; and (3) it does not need to achieve hundreds of thousands of RPM to meet the fuel cell anode pressure rise demand. However, its only drawback is low efficiency. As was previously analysed, the future development trend of hydrogen recirculation devices is ejectors in parallel with blowers. The ejector can realize the hydrogen recirculation in the fuel cell in the middle- and high-power conditions, and the small power operating conditions can be compensated for by a mechanical blower. When the regenerative blower is connected in parallel with the ejector, the ejector is used to realize hydrogen recirculation under the middle- and high-power conditions of the stack. The regenerative blower can stably run in low-power operation mode under a small flow rate, and despite the low efficiency of the single regenerative blower, the whole recirculation system does not suffer from too high energy consumption.

Research on the use of regenerative blowers in fuel cell hydrogen recirculation is very slight. Kim et al. [48] used a CFD method to study the characteristic of a hydrogen regenerative blower and improved the accuracy of the performance prediction by correcting the loss model. Badami et al. [49] established a one-dimensional model of a hydrogen recirculation regenerative blower for an automotive PEMFC by simply modifying the one-dimensional model. The theoretical model was experimentally validated and the performance of the blower was predicted reasonably and accurately. The authors also provided a substantial contribution to the rapid design of this type of blower. After that, Badami et al. [50] investigated the impact of leakage for an automotive PEMFC regenerative-type hydrogen delivery blower, indicating that the performance of the blower rapidly decreased with the increase in the gap. Three-dimensional CFD analyses were also carried out by Badami [51], which not only provided a better understanding of the regenerative blower's internal fluid dynamics, but the CFD analysis results can also be compared with the one-dimensional theory to analyse the assumptions made in the previous one-dimensional model. Although the optimization of the hydrogen regenerative blower is especially important because of its low efficiency, the optimization of the flow path of the hydrogen regenerative blower has not been yet reported in the literature. The response



surface methodology (RSM) is a proven method to research the interaction between different factors, and it is capable of determining the relationship between different variables [52]. The RSM, in combination with the CFD simulation and genetic algorithm (GA), has been used to perform geometrical–structural interaction analysis and the geometrical parameter optimization [53–58]. Under this perspective, the aim of this work is to improve the efficiency of a hydrogen regenerative blower by performing geometrical optimization and reveal the influence of geometric parameters on the performance of the regenerative blower. In this work, a three-dimensional CFD model of the regenerative blower was first established and experiments were conducted to verify the accuracy of the model. The range of the dimensional parameters was selected according to the actual application, and the impact of single-factor geometrical parameters on the performance was first analysed. After that, the interactions between the different geometrical factors were researched using the central composite design (CCD) and the RSM methods. Additionally, a regression model was developed by means of the RSM results, and the regression model was solved using a genetic algorithm (GA), as a result, a globally optimal solution for the geometrical sizes of the hydrogen regenerative blower is obtained. The effectiveness of the optimized results was validated by carrying out CFD solutions, and the entropy generation distributions in the internal flow field of the original design and the optimized design were compared and analysed. Finally, it was found that the efficiency of the optimized regenerative blower was significantly improved under different operating conditions.

## 2. Methods

As can be seen in Figure 2, a regenerative blower generally consists of an impeller and a casing. The former contains vanes around the impeller, and the latter has a machined side channel with the inlet and outlet ends separated by a septum. In the past, two theories have mainly developed to analyse the principle of the regenerative blower: namely, the turbulent theory and the momentum exchange theory. Later, based on a large number of experimental studies, it was found that the momentum exchange theory is more accurate. More specifically, as the fluid flows from the inlet to the outlet ports, it will undergo the impact of meridional circulatory motion generated by the centrifugal field of the impeller. Therefore, the fluid goes into the vane grooves several times to increase its angular momentum. When the fluid enters the side channel, it will be mixed with the fluid inside the channel, and as a result, the pressure of the fluid inside will be increased [59]. As shown in Figure 3, the fluid motion inside the regenerative blower can be described by two components: the tangential component of the flow determines the effective flow rate  $Q$  and the meridional component determines the recirculation flow rate  $Q_m$ . Table 1 lists the anode pressure drop and flow rate parameters of the fuel cell stack, and Case 5 is the design point. According to the design point operating conditions, a radial vane hydrogen recirculation regenerative blower for automotive fuel cells was designed based on the momentum exchange theory, and its main geometrical parameters and schematic diagrams are depicted in Figure 4 and Table 2.

**Table 1.** PEMFC anode pressure and flow conditions.

Case	Anode Inlet Gauge Pressure (kPa)	Anode Outlet Gauge Pressure (kPa)	Pressure Drop (kPa)	Anode Outlet Flow ( $\text{g s}^{-1}$ )
1	95	86	9	1.8
2	115	106	9	2.17
3	125	116	9	2.53
4	125	114	11	2.89
5	135	120	15	3.24
6	141	124	17	3.61
7	145	126	19	3.97

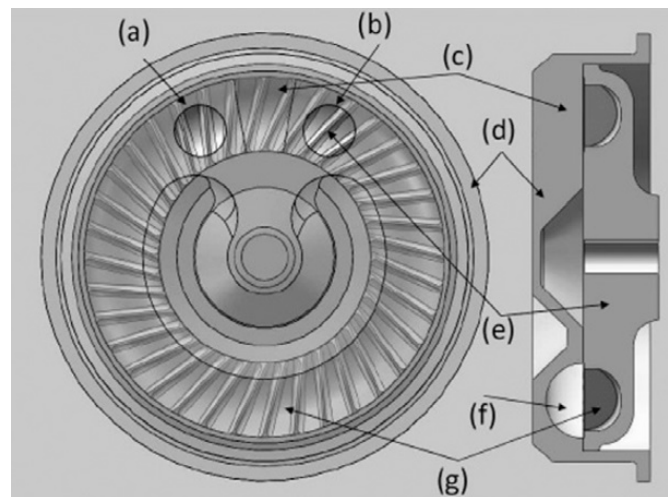


**Figure 2.** Regenerative blower parts: (a) inlet, (b) outlet, (c) septum, (d) casing, (e) impeller, (f) side channel, and (g) vanes [51].

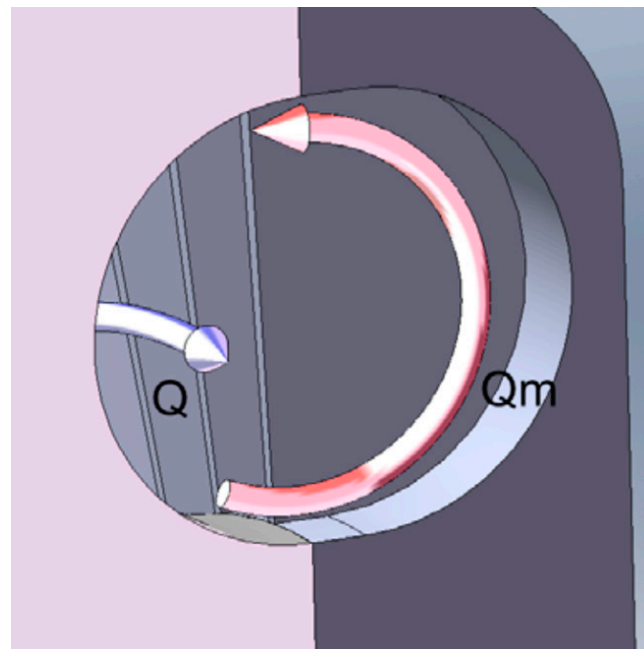


**Figure 3.** Circulatory flow rate  $Q_m$  (in red) and flow rate  $Q$  (in blue) [49].

**Table 2.** Main characteristics of the initial regenerative blower.

Parameters	Unit	Value
External radius of the impeller, $r$	mm	60
Inner radius of the impeller, $r_i$	mm	35
Number of vanes, $z$	/	40
Thickness of the vanes, $t$	mm	1.5
Angle of the vanes, $\theta$	°	90
Height of the vanes, $h$	mm	25
Width of the vanes, $w$	mm	12.5
Height of the side channel, $h_c$	mm	25
Width of the side channel, $w_c$	mm	12.5
Angle of the septum, $\theta_s$	°	30
Axial clearance, $G$	mm	0.2

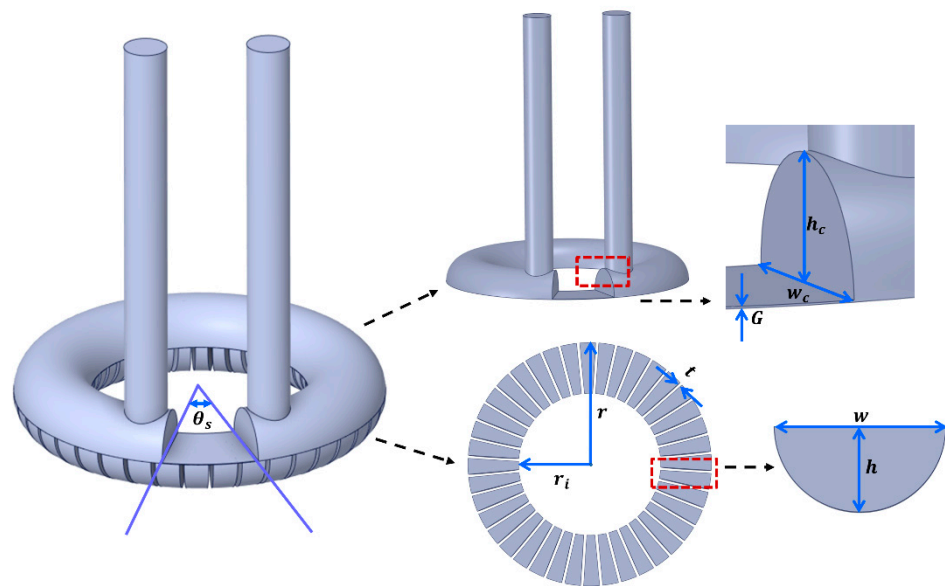


**Figure 4.** Schematic diagram of the geometric parameters.

### 2.1. CFD Numerical Models

A three-dimensional CFD model of the PEMFC regenerative blower was developed by means of ANSYS Fluent 2021R1. Since the present analysis only focuses on steady-state results, the “Multiple-Reference-Frame (MRF)” technique was considered the most appropriate because more satisfactory results on the mechanical properties of the impeller can be obtained, with high stability and a short computational time, in terms of pressure ratios, mass flow rates, and efficiencies. In dealing with the flow from the rotating domain to the stationary domain (or vice versa), the MRF model was realized by changing the reference system while maintaining the relative positions of these fluid domains. This method is characterized by high stability and uses less computational resources compared to other methods [60].

#### 2.1.1. Simulation Assumptions

To simulate the flow inside the hydrogen regenerative blower of the PEMFCs, the following assumptions were made:

1. The fuel cell anode exhaust is regarded as an ideal gas and its state parameters satisfy the ideal gas equation:

$$P = \rho RT \quad (1)$$

where  $P$  is the absolute pressure,  $\rho$  denotes the density,  $R$  refers to the specific gas constant, and  $T$  represents the temperature.

2. The condensation of the water vapour inside the regenerative blower was ignored, so the internal flow in the blower is in a single phase.
3. The internal flow rate inside the regenerative blower is very fast, and the fluid does not have time to heat transfer, so it was assumed that the internal walls are adiabatic.
4. The gravity of gas molecules from the anode outlet was ignored.

#### 2.1.2. Governing Equations

The steady turbulent flow was used to describe the internal flow of the regenerative blower, and the high-speed internal flow was compressible. Several conservation equations are listed below:

Mass conservation:

$$\nabla(\rho \vec{u}) = 0, \quad (2)$$

Momentum conservation:

$$\nabla(\rho u_i \vec{u}) = -\frac{\partial P}{\partial x_i} + \left( \frac{\partial \tau_{ii}}{\partial x_i} + \frac{\partial \tau_{ji}}{\partial x_j} + \frac{\partial \tau_{ki}}{\partial x_k} \right) + \rho f_i, \quad (3)$$

Energy conservation:

$$\nabla(\vec{u}(\rho E + P)) = \nabla \left[ k_{eff} \nabla T - \sum_c h_c J_c + (\tau \cdot \vec{u}) \right], \quad (4)$$

Species transport equation:

$$\nabla(\rho \vec{u} Y_c) = -\nabla J_c, \quad (5)$$

where  $\vec{u}$  is the velocity vector;  $i, j$ , and  $k$  stand for the directions;  $\tau$  is the stress tensor;  $E$  is total energy;  $f$  is the mass force;  $k_{eff}$  refers to the effective thermal conductivity;  $h_c$  is the enthalpy of species  $c$ ;  $J_c$  represents the diffusive flux of species  $c$ ; and  $Y_c$  denotes the mass fraction of species  $c$ .

The turbulence model is an additional equation to solve the Navier–Stokes equation. The shear stress transport (SST)  $k$ - $\omega$  turbulence model was adopted, which shows satisfactory accuracy in the simulation calculation of other types of regenerative blowers [51,61–63]. The governing equations are as follows:

$$\frac{\partial}{\partial x_i}(\rho k v_i) = \frac{\partial}{\partial x_j} \left( \Gamma_k \frac{\partial k}{\partial x_j} \right) + G_k - Y_k \quad (6)$$

$$\frac{\partial}{\partial x_j}(\rho \omega v_j) = \frac{\partial}{\partial x_j} \left( \Gamma_\omega \frac{\partial \omega}{\partial x_j} \right) + G_\omega - Y_\omega + D_\omega \quad (7)$$

where  $\Gamma_k$  and  $\Gamma_\omega$  refer to the effective diffusivities of  $k$  and  $\omega$ , respectively;  $G_k$  and  $G_\omega$  stand for the production rates of  $k$  and  $\omega$ , respectively;  $Y_k$  and  $Y_\omega$  represent the diffusivities of  $k$  and  $\omega$ , respectively; and  $D_\omega$  is the transverse diffusion term of  $\omega$ .

The above control equations were solved using a pressure-based coupled solver, and the discretization of momentum, components of species transport, turbulent kinetic energy, and turbulent dissipation rate were all in a second-order scheme.

### 2.1.3. Boundary Conditions

The PEMFC anode outlet is located at the inlet of the hydrogen regenerative blower, and the components and proportions of the mixed gas in the anode exhaust are presented in Table 3. The inlet boundary condition adopts the pressure inlet and the outlet boundary condition adopts the mass flow outlet, and the boundary condition settings are shown in Table 4. The target pressure rise of the blower was 15 kPa, and the user-defined function (UDF) was used to automatically adjust the speed until the pressure difference between the inlet and outlet was stabilized at 15 kPa.

**Table 3.** Components and proportions of the mixed gas.

Components of the Mixed Gas	Mole Fraction
Hydrogen	0.78
Water vapour	0.15
Nitrogen	0.07

**Table 4.** Boundary conditions.

Boundary	Type	Values
Inlet	Pressure inlet (gauge pressure) (kPa)	120
	Inlet temperature (K)	338.15
Outlet	Mass flow outlet ( $\text{g s}^{-1}$ )	3.24

#### 2.1.4. Model Validation

The experimental testing of the regenerative blower was carried out in the Kaigrisen laboratory using a rig, as shown in Figure 5, and a schematic diagram of the rig is as displayed in Figure 6. The basic procedure of Figure 6 can be described as follows: First, the operator should open the manual valve. Then, the air compressor should be started so that the air enters into the main line. The compressed air after the filter moves in two directions. One way is through the pressure-reducing valve as the control air source of a pneumatic backpressure valve. The other way is through the pressure-reducing valve, the pressure gauge, the safety valve, and the solenoid valve in sequence. At last, the air source is regarded as a test gas of the recirculation blower to measure the external characteristics. The pressure rise and mass flow characteristics of the regenerative blower at different rotational speeds can be obtained from the bench. The rotational speed was regulated by a computerized direct control motor controller. Both the inlet and outlet gauge pressure can be measured by capacitive absolute pressure transmitters; the measurement range of the pressure transmitters was 0–500 kPa, and the maximum permissible error was  $\pm 0.5\%$ ; the import and export temperatures were measured by using a resistance temperature detector (RTD) temperature sensor, where the measurement range was 0–120 °C, and the maximum permissible error was  $\pm 1$  °C; the mass flow rate was obtained from the ultrasonic flowmeter (F), where the measurement range was 15–1500 SLPM, and the maximum permissible error was  $\pm 0.1\%$ .

**Figure 5.** Test rig for the regenerative blower.



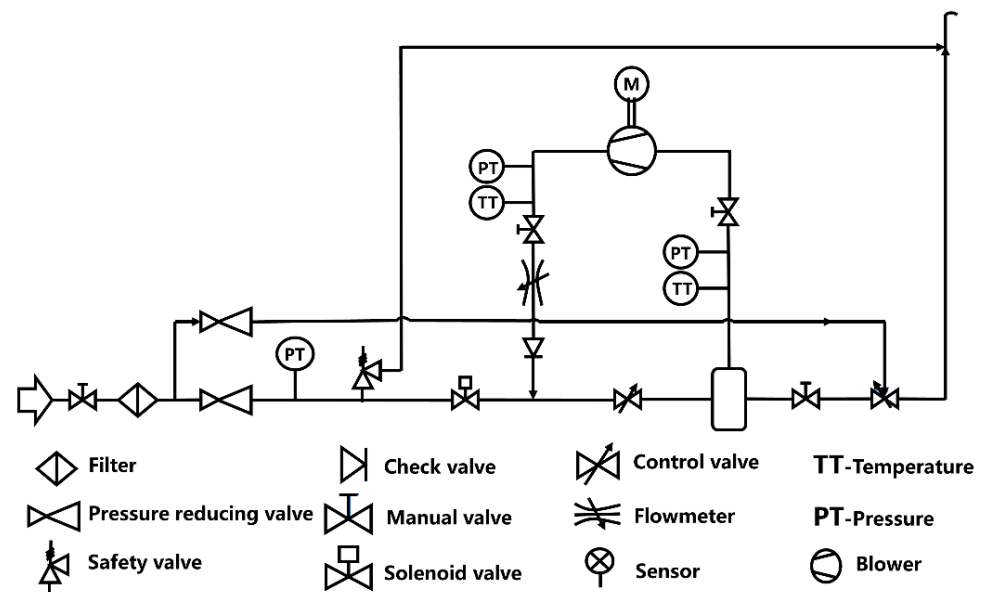


Figure 6. Schematic diagram of the rig.

To verify the accuracy of the CFD model, experiments with compressed air were carried out. The experiments were conducted by measuring the inlet and the outlet pressure rise at different speeds (9000–17,000 RPM) and flow rates (511.3–1143 SLPM) and comparing them with the results obtained by performing CFD simulations under the same conditions, as shown in Figure 7. The results showed that the average error between the simulation and the experiment was 3.4155%, and the maximum error did not exceed 7%. These errors can be attributed to the experimental and processing errors of the regenerative blower. Therefore, the accuracy of the established CFD model is acceptable.

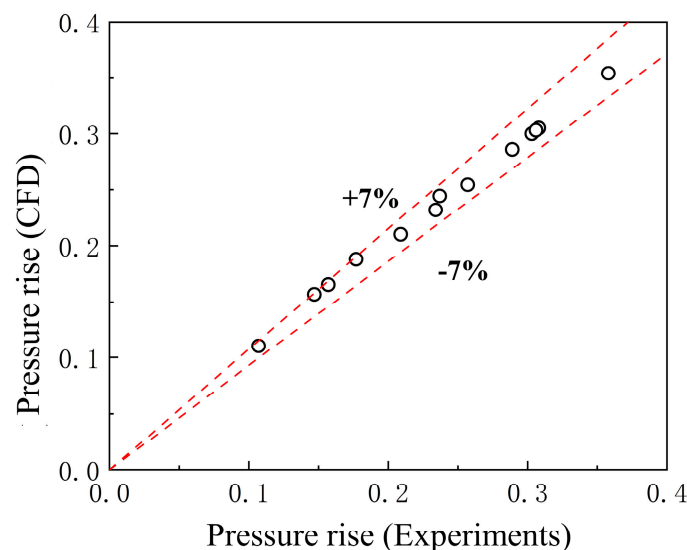


Figure 7. Comparisons of the pressure rise between the experimental and CFD data.

## 2.2. Response Surface Methodology (RSM)

Although the hydrogen regenerative blower has a simple structure, its internal flow is very complicated, and the RSM is a reliable way to obtain a regression model between the geometrical sizes and the performance of the regenerative blower. First, the factors and levels of RSM should be determined, followed by conducting a design of experiments (DOE). As the most commonly used DOE method in RSM [52], the central composite design is adopted in this paper. Considering the compactness requirement of the fuel cell

system, the maximum outer radius of the impeller of the regenerative blower was selected to be 60 mm. When the pressure rise is the same, a larger outer diameter of the impeller corresponds to a smaller rotational speed [64]. In practice, to improve the reliability and life of the motor, it should be run at the lowest possible rotational speed, so the outer radius of the impeller of the regenerative blower was fixed at 60 mm. According to the operation principle of the regenerative blower described above, the internal recirculation flow runs in a spiral-shaped pattern between the impeller groove and the side channel. For this reason, the size of the vane height was set the same as the side channel height, which ensures that the coherence of the flow was increased and resistance was reduced. Therefore, in this work, six factors, namely, number of blades ( $X_1$ ), blade thickness ( $X_2$ ), blade inclination ( $X_3$ ), blade height ( $X_4$ ), septum angle ( $X_5$ ), and impeller inner radius ( $X_6$ ) were selected as the independent variables, and the experimental points were generated by using the face-centred composite design method, which can meet the requirements of establishing a response surface model but has the advantages of fewer runs and less computation time [49]. All independent variables were investigated at the levels of  $-1$ ,  $0$ , and  $1$ . The software JMP Pro V16.0 was applied for the six-factor, three-level CCD experimental design to generate 46 groups.

The efficiency of the regenerative blower is the ratio of the output work to the input work, the output work can be calculated from the inlet and the outlet differential pressure and flow rate, and the input work can be calculated from the rotational speed and torque [64] as shown in Equation (8). The objective of this work was to maximize the efficiency of the regenerative blower to minimize the power consumption of the hydrogen recirculation unit, so the efficiency was chosen as the response variable ( $Y$ ) in this work.

$$\eta = \frac{P_{output}}{P_{input}} = \frac{Q * P_{diff}}{N * RPM * 3.14 * \frac{2}{60}} \quad (8)$$

The corresponding 46 sets of test conditions were calculated using CFDs. The 46 sets of independent variables, as well as their response variables, were written into a table, and JMP Pro V16.0 was applied to perform an analysis of variance (ANOVA) and fit a second-order model with the simulated data. The second-order polynomial response surface model is depicted in Equation (9).

$$Y = \beta_0 + \sum_{i=1}^6 \beta_i X_i + \sum_{i < j} \beta_{ij} X_{ij} + \sum_{i=1}^6 \beta_{ii} X_{ii} \quad (9)$$

where  $X$  is the independent variable,  $Y$  refers to the response variable, and  $\beta_0$ ,  $\beta_i$ ,  $\beta_{ij}$ , and  $\beta_{ii}$  represent the coefficients of the intercept, linear, interaction, and quadratic terms, respectively [65].

To achieve the maximum value of the above established response surface model and the optimal configuration of the geometric variables, a genetic algorithm was used to solve the model. The genetic algorithm can be described as a random search and global optimization method, and it is generally used to solve multivariate optimization problems. The agent model function of the genetic algorithm of this work was an empirical regression model generated by RSM. The optimal geometric parameters and maximum blower efficiency acquired by the genetic algorithm were verified by performing CFD simulations. The reliability of the RSM and the genetic algorithm optimization is acceptable if the difference between the genetic algorithm results and the CFD results is less than 5%, and the error is defined as shown in Equation (10). The whole RSM and GA optimization flowchart is illustrated in Figure 8.

$$\delta = \frac{\eta_{GA} - \eta_{CFD}}{\eta_{CFD}} \times 100\% \quad (10)$$

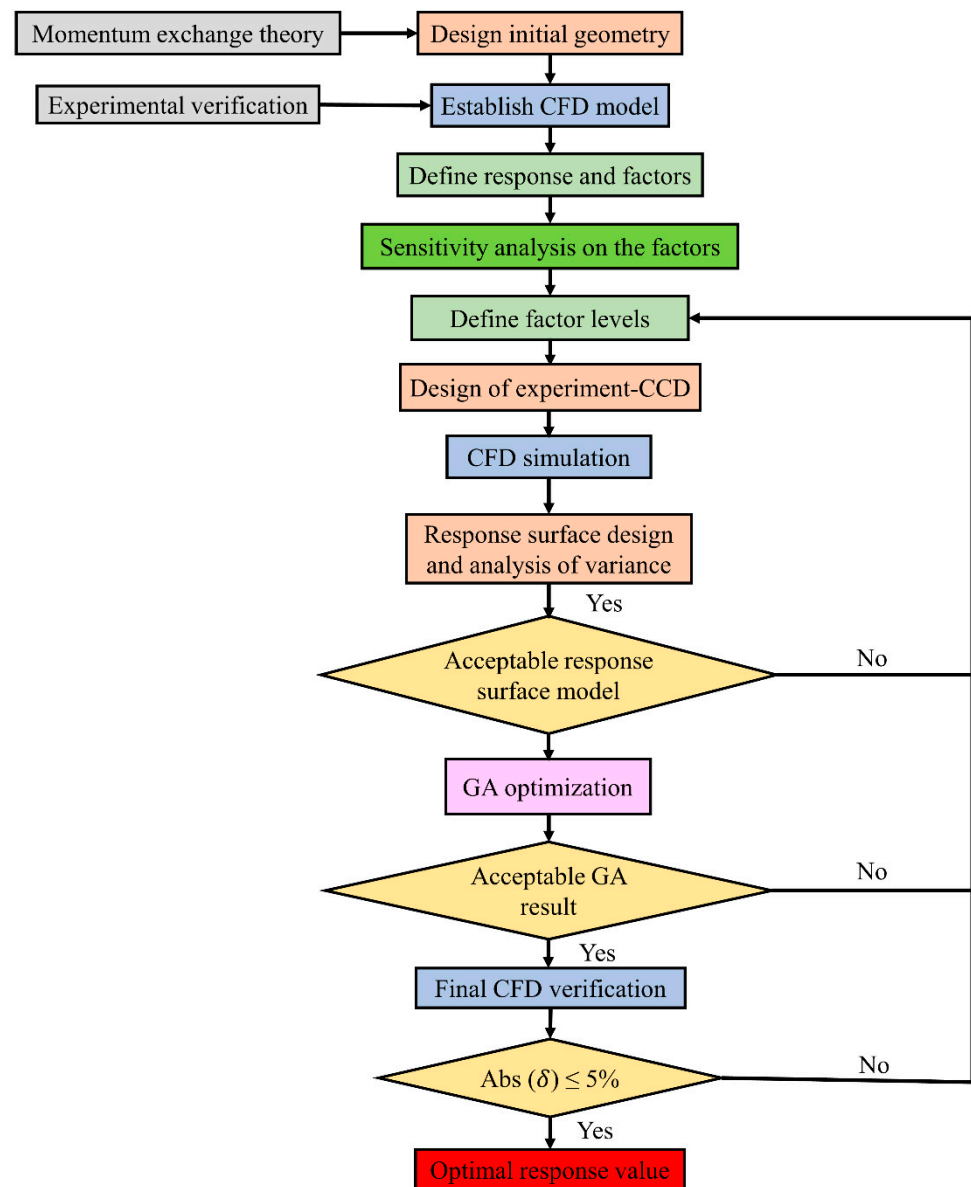


**Figure 8.** Optimization flowchart of GA and RSM.

### 3. Results and Discussion

#### 3.1. Single-Factor Analysis of the Geometry Parameters

The rated operating point of the fuel cell stack is Case 5 in Table 2, and the initial geometry of the regenerative blower was designed based on the rated operating point. Therefore, this point was used for a one-factor analysis. The other geometric parameters were fixed to maintain the preliminary design geometry when conducting the single-factor analysis.

##### 3.1.1. Impact of the Vane Number

According to Streekanth's study [64], the majority of the reported works in the literature use a vane number range of 30–50 and the number of vanes in the initial geometry was 40. Thereby, the vane number range of 30–50 was also selected in this work. As shown in Figure 9, the efficiency of the regenerative blower decreased as the number of vanes increased from 30 to 50.

The existence of a higher number of vanes leads to a reduction in the slip coefficient, which results in a regenerative blower performance closer to its design point. However, a higher number of vanes increases the contact area between the fluid and the wall, which

will cause excessive friction losses. Therefore, the vane number must be appropriately obtained. In addition, the fluid inside the blower repeatedly enters and leaves the vane groove many times; due to the shear characteristics of the flow inside the regenerative blower, the increase in the number of vanes will reduce the volume of the vane groove and create greater resistance.

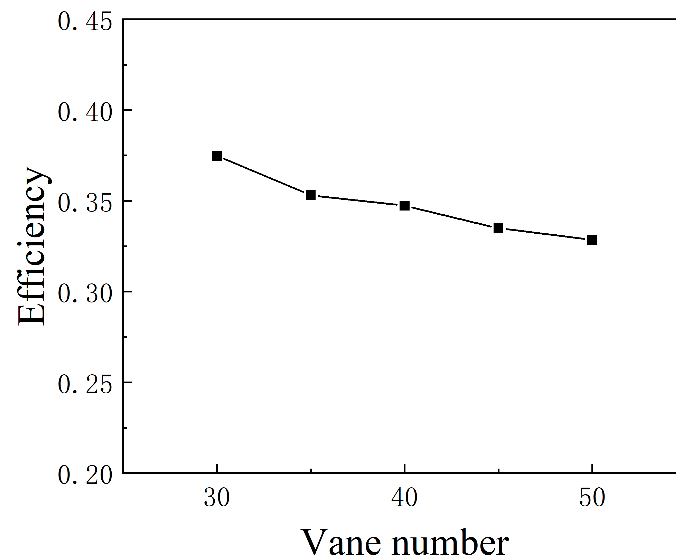


**Figure 9.** Simulated efficiency for different vane numbers.

### 3.1.2. Impact of the Blade Thickness

Considering the actual processing and blade strength, the minimum blade thickness that can be realized is 1.2 mm and the initial design of the blade thickness is 1.5 mm, so the selected blade thickness range is 1.2–1.8 mm. With the increase in the blade thickness, not only does the impeller groove volume decrease, but also the effective meridian area of the side channel is reduced, and less circulatory flow rate transfers momentum to the gas inside the side channel, resulting in the reduced performance and efficiency of the regenerative blower, as can be seen from Figure 10. Therefore, during the actual operation, the vane thickness should be as small as possible.

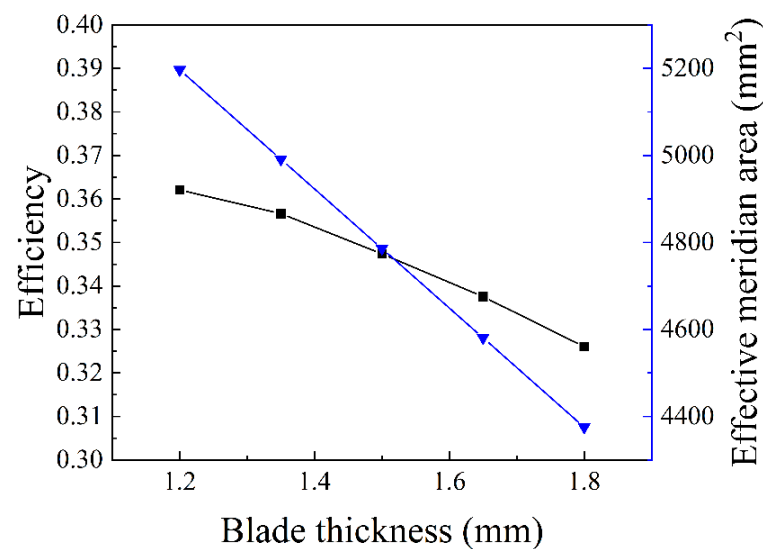


**Figure 10.** Simulated efficiency and effective meridian area for different blade thicknesses.

### 3.1.3. Impact of the Blade Angle

The preliminary design uses radial blades with  $90^\circ$ , and according to Badami's study [44], the blade inclination range of  $65^\circ$ – $115^\circ$  was selected in this work. The velocity cloud of the middle-height section of the blade is shown in Figure 11. Under the condition that the rotational speed, impeller radius, and flow rate are all the same, the average velocity of the middle section of the impeller of the forward-curved blade ( $65^\circ$ ), radial blade ( $90^\circ$ ), and backward-curved blade ( $115^\circ$ ) gradually decreases. Moreover, the absolute velocity of the forward-curved impeller is higher than that of the backward-curved one, while the flow loss is directly proportional to the square of the velocity, so that the forward-curved blade is the most inefficient. According to Badami's study [46], the recirculation flow from near the inner diameter of the impeller to the outer diameter produces a similar helix vortex flow. If the blade's backward-bending angle is too large, it will lead to a reduction in the flow area near the inner diameter of the impeller. Consequently, the flow area at the outer diameter of the impeller will be increased, and the flow losses will be also increased due to the area imbalance induced by the entrance and exit of the vane grooves of the circulatory flow rate. Therefore, as shown in Figure 12, when the blade bending angle is  $102.5^\circ$ , the blade efficiency is the highest instead of  $115^\circ$ .

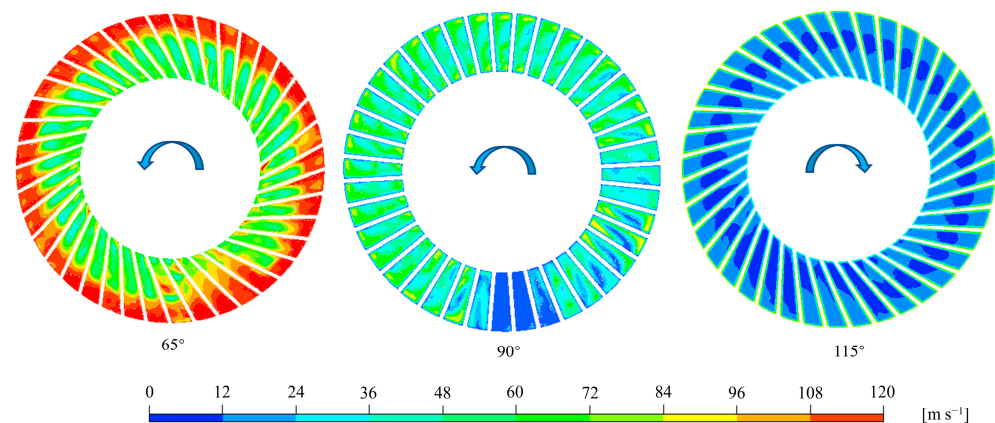


**Figure 11.** Velocity contour in the middle section of the impeller at  $65^\circ$ ,  $90^\circ$ , and  $115^\circ$  angles.

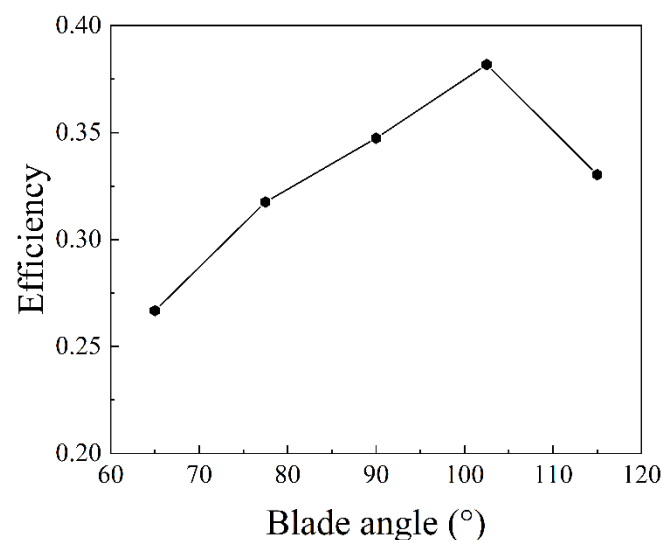


**Figure 12.** Simulated efficiency for different blade angles.

### 3.1.4. Impact of the Blade Height

If the height of the blade is too large, it cannot meet the compactness requirements of the fuel cell system. On the contrary, if the blade height is too small, the internal flow



path will be reduced, resulting in a large flow velocity and high motor speed. A high flow velocity will induce a large flow loss because it is proportional to the quadratic of velocity. In the meantime, a too-high speed has an adverse effect on the design and operation of the motor and bearings, and the initial design size of the blade height is 12.5 mm; considering the above, the selected blade height range is 6–19 mm. With the increase in the blade height, the recirculation is increased in the flow path, which not only induces a route loss along with the path growth, but also the recirculation flow inside the impeller groove cannot transfer the momentum to the gas in the side channel faster. In addition, the recirculation flow inside the side channel cannot flow into the impeller groove in time to obtain the momentum of the impeller. Therefore, as shown in Figure 13, the efficiency of the regenerative blower gradually decreased when the height of the impeller increased from 6 mm to 19 mm.

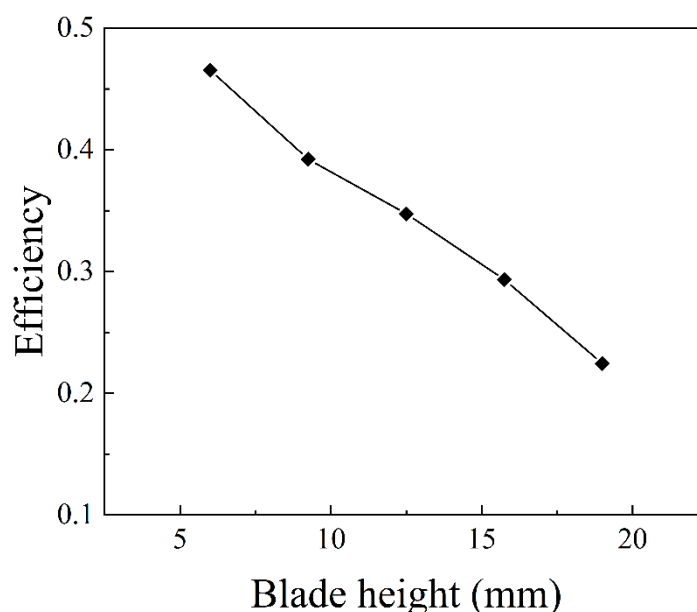


**Figure 13.** Simulated efficiency for different blade heights.

### 3.1.5. Impact of the Septum Angle

If the septum angle is too small, the processing and manufacturing of the inlet and outlet ports is hindered. On the contrary, if the angle is too large, the effective momentum exchange area of the regenerative blower will be also reduced, and the initial geometry of the septum angle will be 30°. Given the above-mentioned analysis, the selected septum angle range is 20–40°. Usually, a smaller septum angle leads to a greater effective meridian area of the regenerative blower, and a stronger momentum exchange between the circulatory flow and the flow inside the side channel, which will make the efficiency of the regenerative blower continue to improve. However, the hydrogen molecules are very easy to leak, and the smaller septum angle will lead to a shorter leak path between the inlet and the outlet caused by the axial gap. As a result, the leakage will be more serious, and the performance of the pump will also decline. Therefore, as shown in Figure 14, when the septum angle ranges within 20–40°, the efficiency of the regenerative blower is almost unchanged. Thus, it can be considered that the impact of the meridian area's change and the leakage between the inlet and the outlet is balanced.

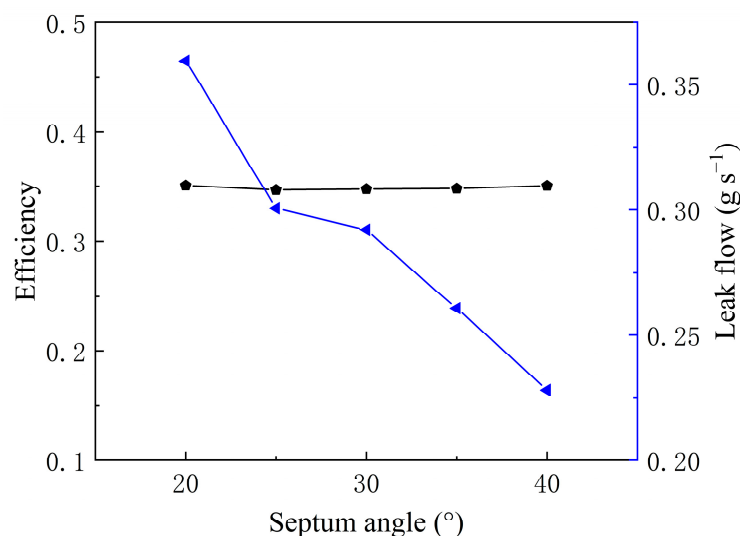


**Figure 14.** Simulated efficiency and effective meridian area for different septum angles.

### 3.1.6. Impact of the Impeller Inner Radius

In practice, the motor magnetic cylinder is located in the middle of the regenerative blower. If the impeller's inner radius is too small, the middle of the blower volume will also be too small and the magnetic cylinder cannot be installed; if the size is too large, because the outer diameter size is fixed due to the fuel cell system compactness requirements, the internal flow channel will be smaller, resulting in a large loss of the high flow velocity of the fluid. The initial design size of the inner radius is 35 mm, and the selected impeller inner diameter range is 25–45 mm after comprehensive consideration. When the outer radius and the other parameters remain unchanged, the existence of a larger inner radius of the impeller not only induces the circulatory flow to enter and leave the impeller groove cross-section more uniform, but also shortens the spiral flow of the path. A smaller flow loss, at the same time, induces also a smaller leakage area caused by the axial clearance between the inlet and the outlet clearance. Hence, the leakage rate will be also reduced, which will increase the efficiency of the regenerative blower. However, when the inner radius increases to a certain extent, the overall structure of the blower and the internal flow path will become smaller. Taking into account that the import and export flux are constant, it will lead to an increase in both the internal flow velocity and the loss. At the same time, the entire volume of the impeller grooves will decrease, resulting in a reduction in the momentum acquired by the recirculation flow from the blade. Then, the momentum transferred by the recirculation flow to the fluid inside the side channel will also consequentially decrease. Therefore, as depicted in Figure 15, when the inner radius of the impeller is increased from 25 mm to 40 mm, the efficiency of the regenerative blower shows a trend of increasing and then decreasing. As shown in Figure 16, the velocity direction in the lower left part of the middle impeller groove in (a) is particularly messy, which means that the fluid inside the impeller is subjected to a large energy loss and cannot transfer the momentum to the fluid in the side channel efficiently. In (b), the velocity direction of the fluid in the side channel near the parting interface is significantly deviated, and cannot go into the impeller groove to obtain better momentum. The vortex area in the middle of the impeller groove of (c) is too large, and the flow loss is also large. In image (e), the fluid reflux is more intense in the middle impeller groove and the side channel, and the area of momentum exchange at the interface is small, resulting in low momentum conversion efficiency. Therefore, the efficiency of the impeller with an inner radius of 40 mm, namely (d), is the highest.

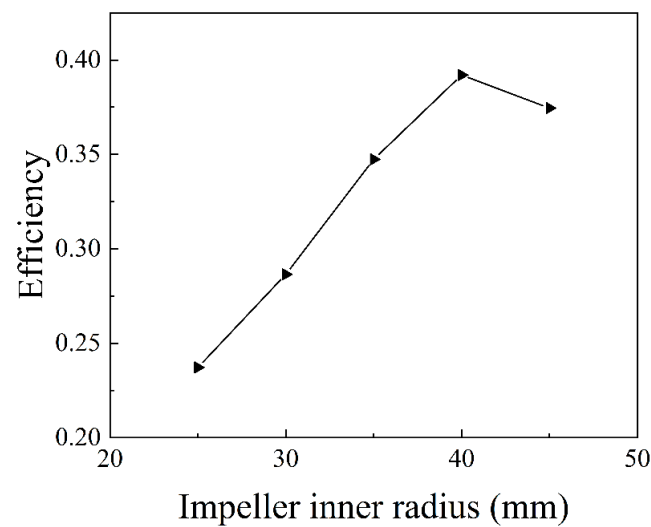


Figure 15. Simulated efficiency for different impeller inner radii.

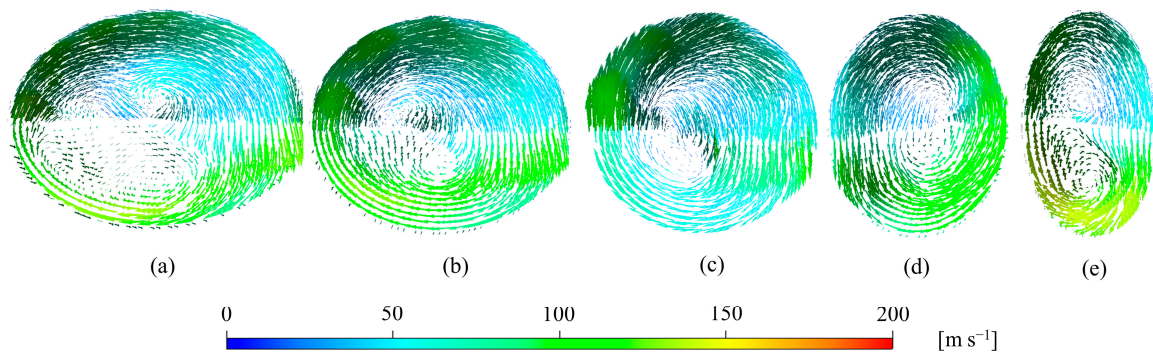


Figure 16. Velocity vector diagram for different impeller inner radii: (a) 25 mm, (b) 30 mm, (c) 35 mm, (d) 40 mm, and (e) 45 mm.

### 3.2. Response Surface Analysis

#### 3.2.1. Response Surface Regression Model and ANOVA

The initial values of the geometric parameters of the regenerative blower designed based on the momentum exchange theory were taken as the centre levels as follows: the number of blades was 40, the thickness of the blades was 1.5 mm, the inclination angle of the blades was  $90^\circ$ , the height of the blades was 12.5 mm, the angle of the septum was  $30^\circ$ , and the inner radius of the impeller was 35 mm. The ranges of the six geometric factors according to the previous analysis of the single-factor size selection are presented in Table 5. A total of 46 sets of CCD experimental data were formed by means of JMP Pro V16.0, and the corresponding efficiencies were obtained by CFD. The acquired results are shown in Table 6.

Table 5. Factors and levels of CCD.

Factors	Levels		
	Minimum	Center	Maximum
$X_1$ —blade number	30	40	50
$X_2$ —blade thickness (mm)	1.2	1.5	1.8
$X_3$ —blade angle ( $^\circ$ )	65	90	115
$X_4$ —blade height (mm)	6	12.5	19
$X_5$ —septum angle ( $^\circ$ )	20	30	40
$X_6$ —impeller inner radius (mm)	25	35	45

Table 6. CCD experimental data and simulated efficiency.

Run No.	X <sub>1</sub>	X <sub>2</sub> (mm)	X <sub>3</sub> (°)	X <sub>4</sub> (mm)	X <sub>5</sub> (°)	X <sub>6</sub> (mm)	Efficiency
1	30	1.2	65	6	20	45	0.40928579
2	30	1.2	65	6	40	25	0.200770184
3	30	1.2	65	19	20	25	0.120497948
4	30	1.2	65	19	40	45	0.246498134
5	30	1.2	115	6	20	25	0.341640751
6	30	1.2	115	6	40	45	0.458714092
7	30	1.2	115	19	20	45	0.15887235
8	30	1.2	115	19	40	25	0.173147889
9	30	1.5	90	12.5	30	35	0.348244397
10	30	1.8	65	6	20	25	0.191898097
11	30	1.8	65	6	40	45	0.396547499
12	30	1.8	65	19	20	45	0.243721755
13	30	1.8	65	19	40	25	0.107089095
14	30	1.8	115	6	20	45	0.435775139
15	30	1.8	115	6	40	25	0.363056597
16	30	1.8	115	19	20	25	0.166561326
17	30	1.8	115	19	40	45	0.152661839
18	40	1.2	90	12.5	30	35	0.350472998
19	40	1.5	65	12.5	30	35	0.273482662
20	40	1.5	90	6	30	35	0.441897407
21	40	1.5	90	12.5	20	35	0.348708564
22	40	1.5	90	12.5	30	25	0.25003547
23	40	1.5	90	12.5	30	35	0.34650808
24	40	1.5	90	12.5	30	35	0.34650808
25	40	1.5	90	12.5	30	45	0.361969866
26	40	1.5	90	12.5	40	35	0.352848489
27	40	1.5	90	19	30	35	0.248057191
28	40	1.5	115	12.5	30	35	0.323974013
29	40	1.8	90	12.5	30	35	0.33798766
30	50	1.2	65	6	20	25	0.199783815
31	50	1.2	65	6	40	45	0.445831944
32	50	1.2	65	19	20	45	0.246366933
33	50	1.2	65	19	40	25	0.103496536
34	50	1.2	115	6	20	45	0.479062563
35	50	1.2	115	6	40	25	0.400106285
36	50	1.2	115	19	20	25	0.156971746
37	50	1.2	115	19	40	45	0.184470987
38	50	1.5	90	12.5	30	35	0.355606491
39	50	1.8	65	6	20	45	0.419167978
40	50	1.8	65	6	40	25	0.1893035
41	50	1.8	65	19	20	25	0.09318496
42	50	1.8	65	19	40	45	0.208260261
43	50	1.8	115	6	20	25	0.369632136
44	50	1.8	115	6	40	45	0.475780591
45	50	1.8	115	19	20	45	0.160092546
46	50	1.8	115	19	40	25	0.153019213

The 46 groups of the geometric variables and corresponding efficiency values in Table 6 were then adopted to fit a second-order regression model using JMP Pro V16.0. The significant effects were screened using ANOVA, and a significance level of  $p < 0.05$  standing for a 95% confidence level was adopted for all data. Table 7 shows the conclusions of ANOVA, where the existence of a larger F-value and a smaller  $p$ -value indicate that the effect on the response variable is more significant [66]. It was found that the blade angle ( $X_3$ ), blade height ( $X_4$ ), and inner radius of the impeller ( $X_6$ ) had a significant impact, whereas the effect of blade height was the most significant. Although the main effect of blade number ( $X_1$ ) was not significant, its interaction effects, including  $X_1$  and  $X_4$ , were

statistically different. Therefore, the main effect of  $X_1$  should be also considered in the final model. In addition, as can be seen from Table 7, the  $p$ -values of the quadratic effects of  $X_3^2$  and  $X_6^2$  and the interaction effects of  $X_1 \times X_4$ ,  $X_3 \times X_4$ ,  $X_3 \times X_6$ , and  $X_4 \times X_6$  were all  $<0.05$ , indicating their significant impact and the fact that they should be included in the ultimate model. After gradually removing the insignificant effects, the obtained response surface regression model is shown in Equation (11), and the coefficients of the model are presented in Table 8.

$$Y = \beta_0 + \beta_1 * X_1 + \beta_3 * X_3 + \beta_4 * X_4 + \beta_6 * X_6 + \beta_{33} * X_3^2 + \beta_{66} * X_6^2 + \beta_{14} * X_1 * X_4 + \beta_{34} * X_3 * X_4 + \beta_{36} * X_3 * X_6 + \beta_{46} * X_4 * X_6 \quad (11)$$

**Table 7.** ANOVA of the efficiency.

Source	Sum of Squares	F Ratio	p-Value
Main effect			
$X_1$	0.00046070	1.2295	0.2821 ^
$X_2$	0.00132501	3.5360	0.0763
$X_3$	0.02166970	57.8297	$<0.0001$ *
$X_4$	0.31937925	852.3246	$<0.0001$ *
$X_5$	0.00014568	0.3888	0.5408
$X_6$	0.10649912	284.2133	$<0.0001$ *
Quadratic effect			
$X_1^2$	0.00006979	0.1862	0.6712
$X_2^2$	0.00001234	0.0329	0.8580
$X_3^2$	0.00542872	14.4876	0.0013 *
$X_4^2$	0.00000557	0.0149	0.9043
$X_5^2$	0.00004337	0.1157	0.7376
$X_6^2$	0.00390154	10.4120	0.0047 *
Interaction effect			
$X_1 \times X_2$	0.00028521	0.7611	0.3945
$X_1 \times X_3$	0.00060917	1.6257	0.2185
$X_2 \times X_3$	0.00006889	0.1838	0.6732
$X_1 \times X_4$	0.00186306	4.9719	0.0387 *
$X_2 \times X_4$	0.00000428	0.0114	0.9161
$X_3 \times X_4$	0.02729015	72.8290	$<0.0001$ *
$X_1 \times X_5$	0.00000104	0.0028	0.9585
$X_2 \times X_5$	0.00056843	1.5170	0.2339
$X_3 \times X_5$	0.00043852	1.1703	0.2936
$X_4 \times X_5$	0.00032188	0.8590	0.3663
$X_1 \times X_6$	0.00042138	1.1245	0.3030
$X_2 \times X_6$	0.00017310	0.4619	0.5054
$X_3 \times X_6$	0.03304776	88.1943	$<0.0001$ *
$X_4 \times X_6$	0.01697395	45.2982	$<0.0001$ *
$X_5 \times X_6$	0.00003486	0.0930	0.7639

^ indicates that the main effect is not statistically significant, but a quadratic effect or an interaction effect containing the main effect is statistically significant. \* means the effect was significant.

**Table 8.** Coefficients of the simplified response surface model.

Coefficients	Values	Coefficients	Values
$\beta_0$	−1.63152610063982	$\beta_{66}$	−0.000405054122967807
$\beta_1$	−0.00390063332551235	$\beta_{14}$	−0.000117388373557692
$\beta_3$	0.0200801062130153	$\beta_{34}$	−0.000179710975576923
$\beta_4$	0.0210109275408922	$\beta_{36}$	−0.000128545249375
$\beta_6$	0.0499731432023873	$\beta_{46}$	−0.000354326028365385
$\beta_{33}$	−0.0000764475884748491		



The results of ANOVA also showed that the established model was statistically significant because the  $p$ -value is less than 0.0001. The comparison between the efficiency value calculated by CFD and that predicted by the regression model is depicted in Figure 17. The  $R^2$  of the response surface model was 0.989, the value of adjusted  $R^2$  was 0.972, and the root-mean-square error (RSME) of CFD calculation efficiency and prediction efficiency was 0.0137. When the value of  $R^2$  is closer to 1 and the value of the RMSE is smaller, the model can fit the data better. In other words, the response surface fitting model has good goodness-of-fit on the efficiency of the regenerative blower, and the model can well show the impact of the researched factors on the efficiency, which can be used for the subsequent optimization and evaluation of the regenerative blower.

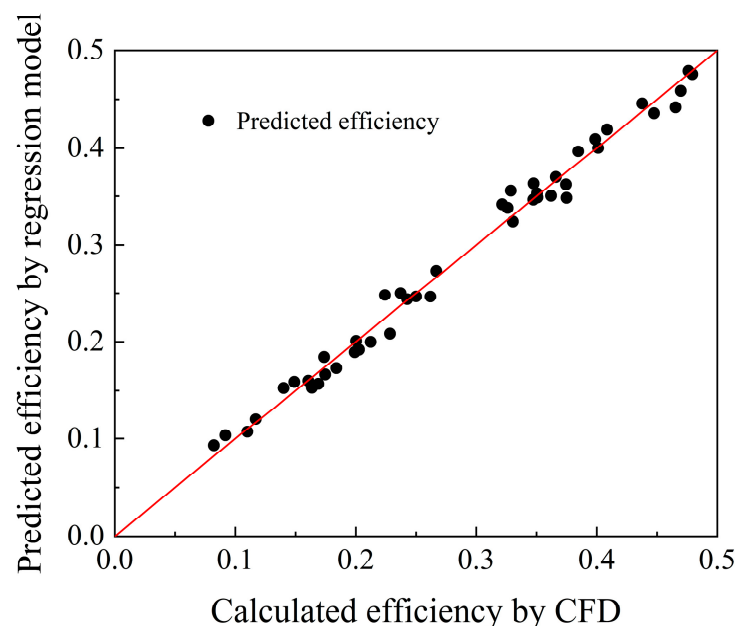


**Figure 17.** Comparison of the efficiency between CFD and regression model.

### 3.2.2. Interaction Effects in Response Surface Figures

Response surface plots can reveal the interaction influence of geometrical parameters on the efficiency. These plots were made by varying two variables while keeping the other independent factors fixed at their initial values. Figure 18a displays the impact of changing the number of blades and blade height on the efficiency. As can be seen, the change in blade height has a greater impact on the efficiency compared to changing the number of blades, while the response surface plots exhibit a relatively small curvature, which suggests that the interaction effect between the two of them is weak. Similarly, as can be observed in Figure 18d, the interaction effect of the blade height and impeller inner diameter is also small, and the efficiency is more sensitive to the change of blade height than the impeller inner radius. However, in Figure 18b,c, the response surface plots have obvious curved characteristics, and the efficiency of the regenerative blower predicted by the regression model increases and then decreases with the increase in the blade angle and the inner radius of the impeller, and the efficiency increases with the decrease in the blade thickness. The convex pattern of the three-dimensional surface indicates that there exists a maximum value of the regression model. This value will be searched in the following section by a genetic algorithm.

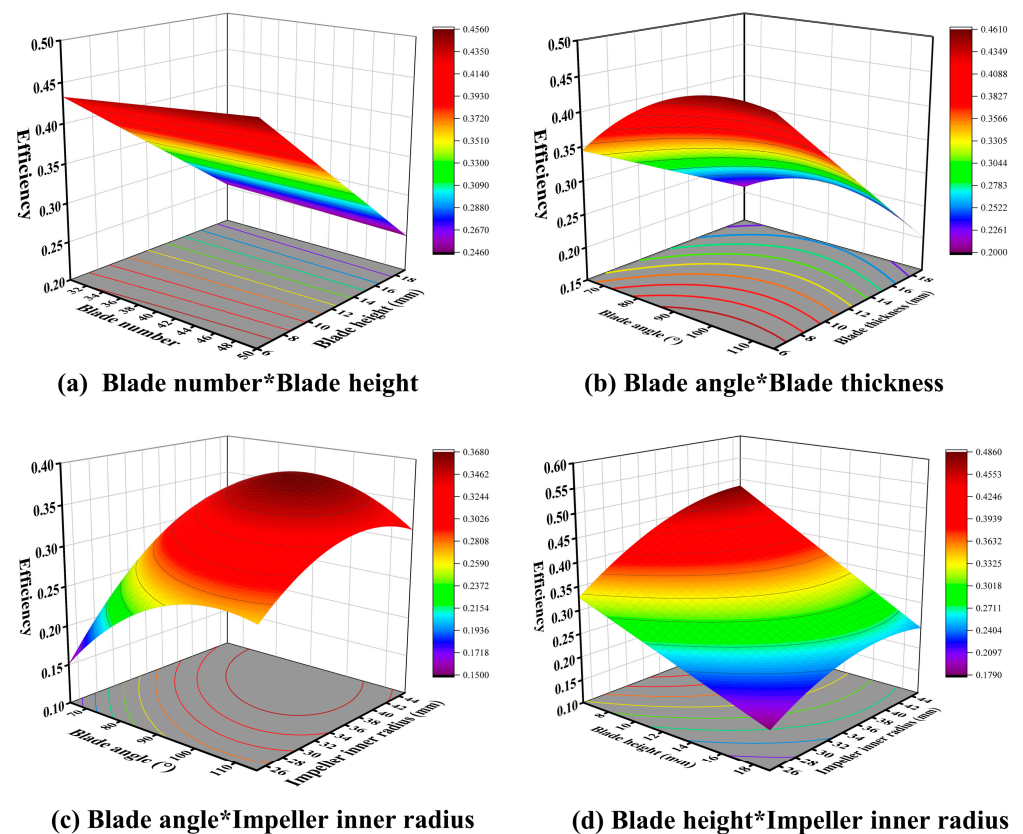


Figure 18. Response surface plots of the predicted model.

### 3.3. Genetic Algorithm, CFD Verification, and Entropy generation Rate Analysis

#### 3.3.1. Genetic Algorithm Optimization

The optimal efficiency of the response surface model was acquired by solving the GA. The GA can only obtain the minimum value of the fitted function. For convenience, the fitting function of the RSM regression model was replaced to be negative. Therefore, the maximum efficiency is the absolute value of the GA optimization result. The MATLAB 2019b GA toolbox [67] was used for carrying out GA optimization.

The GA optimization ended when the average variation in the fitness value was less than the specified functional tolerance  $1 \times 10^{-10}$ . The maximum efficiency obtained by GA was 0.527, and the corresponding geometric values of the blade number, blade thickness, blade angle, blade height, septum angle, and impeller inner radius of the regenerative blower were 50, 1.2 mm,  $98.38^\circ$ , 6 mm,  $40^\circ$ , and 44.03 mm, respectively. The optimized values of the six geometric variables were all within their selected range, indicating that the optimization results of GA are reliable.

#### 3.3.2. CFD Verification and Entropy Generation Rate Analysis

To validate that the results obtained by the above RSM and GA could obtain optimal efficiency, it was required to carry out CFD simulations using the optimized parameters and verify the accuracy of the GA method. The efficiency calculated by CFD was 0.517, and the optimized efficiency calculated by the GA was 0.527. The difference between the CFD calculation and the maximal efficiency acquired by the GA was 1.93%, which is very small and less than 5%. Additionally, the maximum efficiency values after the optimization were all greater than the efficiencies of Table 6, which verifies the effectiveness and correctness of both the RSM and GA methods.

To further study the flow mechanism of the blower and prove the effectiveness of the optimization, the entropy production theory was used to analyse the flow loss distribution inside the impeller. Neglecting the entropy generation of the internal heat transfer because

the velocity inside the blower is very fast, i.e., the internal entropy production of the regenerative blower is mainly generated by viscous dissipation, according to Kock's study [68], the entropy of the viscous dissipation can be divided into average and pulsation terms by using the time-averaged method.

$$S_{gen} = S_{vis} = S_{gen,\bar{D}} + S_{gen,D'}$$

$$S_{gen,\bar{D}} = \frac{2\mu}{T} (S_{ij}S_{ij}) \quad (12)$$

$$S_{gen,D'} = \frac{2\mu}{T} (S'_{ij}S'_{ij})$$

where  $S_{gen,\bar{D}}$  is the entropy generation rate due to direct dissipation,  $S_{gen,D'}$  refers to the entropy generation rate due to turbulence dissipation,  $\mu$  denotes the dynamic viscosity,  $T$  stands for the temperature,  $S_{ij}$  is the strain rate tensor, and  $S'_{ij}$  represents the pulsation strain rate tensor.  $S_{gen,\bar{D}}$  can be directly calculated from the time-averaged quantities in the Reynolds-averaged Navier–Stokes model. Since  $TS_{gen,D'}/\rho$  is the dissipation term of the turbulent kinetic energy transport equation, for the turbulence model used in this work,  $S_{gen,D'}$  was calculated as shown in Equation (13):

$$S_{gen,D'} = \frac{\rho\beta^*k\omega}{T} \quad (13)$$

where  $\beta^* = 0.09$ ,  $k$  is the turbulent kinetic energy, and  $\omega$  states the turbulent eddy frequency.

Figure 19 shows the contour view of the entropy generation rate on the internal wall of the blades, with the initial structure on the left and the optimized structure on the right. As can be seen, the entropy production rate inside the optimized blower was significantly smaller than the initial structure, indicating that the flow loss in the optimized flow channel was reduced. Meanwhile, it can be found from Figure 19a that the loss in the middle part of the vane groove was very large, which can be explained by Figure 20, in which the optimized geometry greatly reduces the internal vortex flow, with a corresponding increase in efficiency due to lower losses. From Figure 19b, we can conclude that the flow loss near the outlet of the impeller surface was particularly large, as shown in the red dotted box. Therefore, further research should be carried out to optimize the outlet port of the regenerative blower.

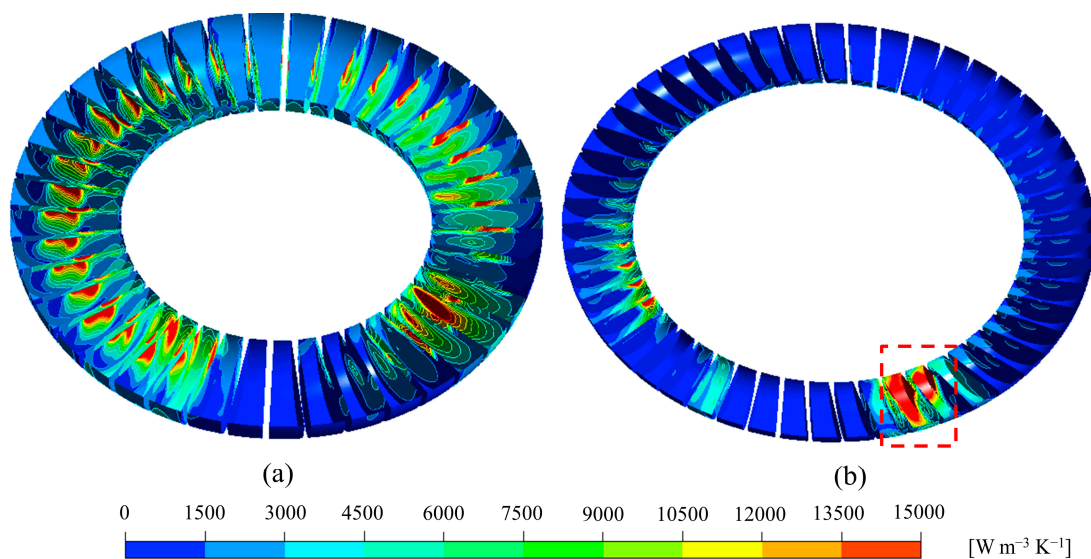


**Figure 19.** Entropy generation rate contour on the internal wall of the blades: (a) initial geometry and (b) optimized geometry.

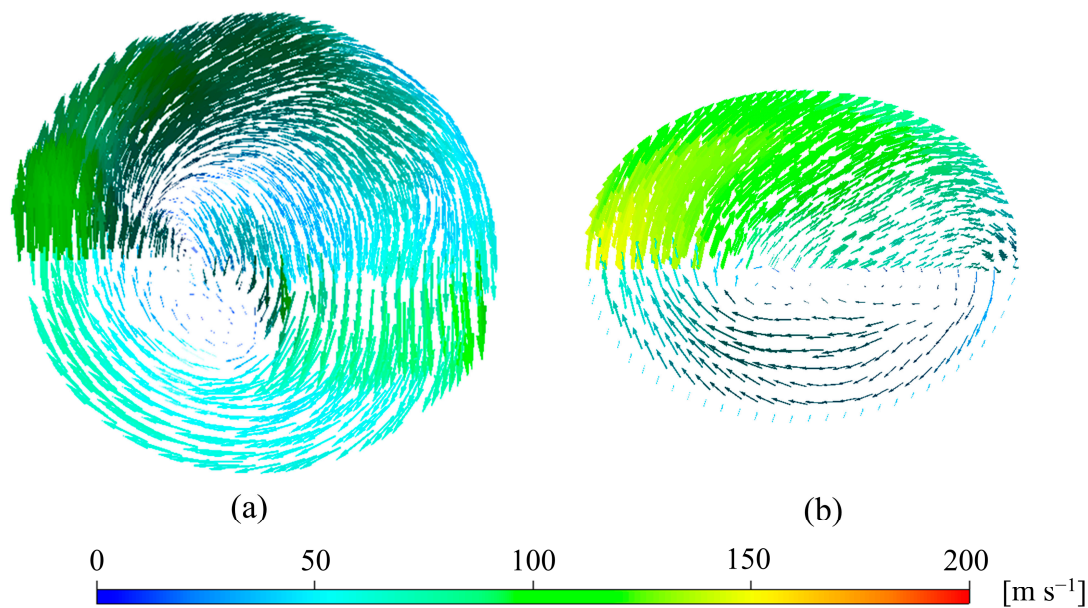


**Figure 20.** Velocity vector diagram for different impeller inner radii: (a) initial geometry and (b) optimized geometry.

### 3.4. Regenerative Blower Efficiency Improvement

The seven Cases from Table 1 were used to validate the increase in the efficiency of the optimized regenerative blower at various operating conditions. Figure 21 illustrates the comparison of the efficiency of the initial and optimized regenerative blowers under different operating conditions. As can be ascertained, the average efficiency of the initial regenerative blower was 34.07%. Such a low efficiency of the initial regenerative blower is due to the excessive internal flow loss caused by the initial structural parameters. On the contrary, the average efficiency of the optimized regenerative blower was 51.61%, which was an improvement of 17.54% compared with the efficiency before optimization, and meanwhile, the efficiency of the optimized regenerative blower at the design point reached 51.7%, which indicates an improvement of 16.95%.

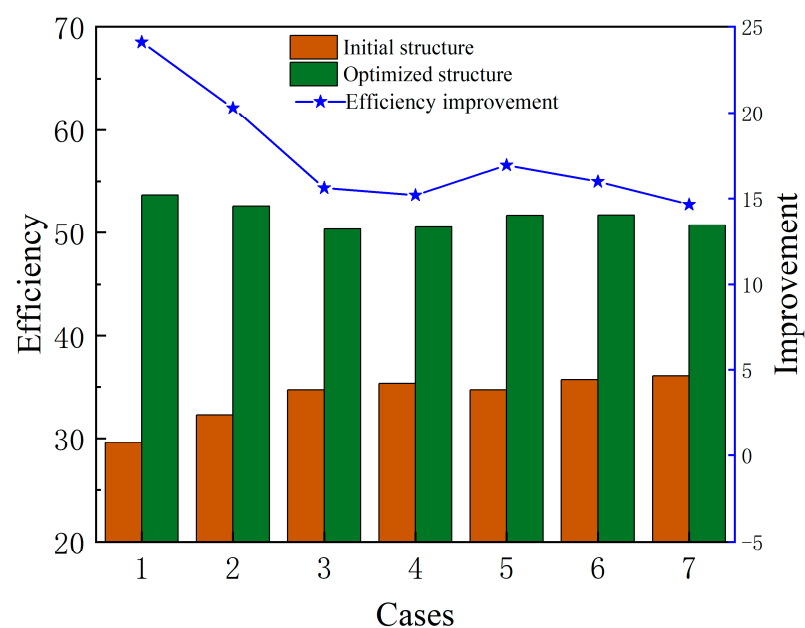


**Figure 21.** Regenerative efficiency of the initial and optimized structure for different operation conditions.

#### 4. Conclusions

In this work, Computational Fluid Dynamics (CFD) techniques, Response Surface Methodology (RSM), and Genetic Algorithm (GA) were well applied to reveal the nonlinear relationship between the performance and the geometric parameters of a hydrogen regenerative blower for PEMFCs, and the structure was optimized. The preliminary dimensions of the regenerative blower were given according to the momentum exchange theory, and a three-dimensional CFD model of the blower was established, the accuracy of which was verified by the collected experimental data. Considering the practical application constraints and similar studies, the six-factor, three-level central composite design (CCD) was determined. After that, the impact of a single geometric parameter on the efficiency was first analysed, and then the interaction between the different geometric parameters was researched by means of RSM and ANOVA. Moreover, a second-order regression model with significant factors was built. Finally, GA was used to seek a solution to the model and obtain the fully optimized geometric dimensions, whereas the reliability of the genetic algorithm results was verified by performing CFD simulations.

The single-geometric analysis showed that the efficiency of the regenerative blower increased and then decreased with the increase in the blade inclination angle and the inner radius of the impeller. From the ANOVA, it was revealed that the impact of blade inclination ( $X_3$ ), blade height ( $X_4$ ), and impeller inner diameter ( $X_6$ ) were significant, with the blade height exhibiting the most significant effect, and the quadratic effects of blade inclination and impeller inner radius were also significant. In addition, the interaction effects of the number of blades with blade height, blade inclination and blade height, blade inclination and impeller inner radius, and blade height and impeller inner radius were all significant. According to the bending characteristics of the three-dimensional response surface plots, it was found that the interaction effects of the number of blades and blade height, and blade height and impeller inner radius, are weaker, blade inclination and blade height were slightly stronger, and blade inclination and impeller inner radius had the strongest interaction effects.

The optimum values for the number of blades, blade thickness, blade Inclination, blade height, septum angle, and impeller inner radius were 50, 1.2 mm, 98.38°, 6 mm, 40°, and 44.03 mm, respectively. The entropy generation analysis of the CFD simulation results concluded that the optimized regenerative blower significantly reduced the internal flow losses and greatly improved its efficiency, which was higher than the cases of the central composite design table, clearly indicating the effectiveness of the RSM and the GA. However, the optimized regenerative blower has large flow losses with a high entropy production rate near the outlet, which should be further studied in the future. Finally, the performance of the optimized blower was improved under different operating conditions of the stack, and the design point efficiency reached 51.7%, which is a significant improvement, and the average efficiency was also increased by 17.54%.

**Author Contributions:** Conceptualization, X.L. and Y.Y.; Methodology, X.L., Y.Q. and J.S.; Software, X.L. and Y.T.; Validation, R.Z. and Y.T.; Investigation, X.L., R.Z. and Y.P.; Resources, Y.Y.; Data curation, Y.P. and Y.Q.; Writing—original draft, X.L.; Writing—review & editing, H.K.; Visualization, J.S.; Supervision, H.K. All authors have read and agreed to the published version of the manuscript.

**Funding:** This research was funded by the National Key Research and Development Program of China (Grant No.2022YFB3505103).

**Institutional Review Board Statement:** Not applicable.

**Informed Consent Statement:** Not applicable.

**Data Availability Statement:** No new data were created or analyzed in this study. Data sharing is not applicable to this article.

**Conflicts of Interest:** Authors Yun Yang, Yunlu Qiu, Yuanxu Tao were employed by the company Shandong Kaigrisen Energy Technology Co., Ltd. The remaining authors declare that the research was conducted in the absence of any commercial or financial relationships that could be construed as a potential conflict of interest.



## Nomenclature

PEMFC	Proton exchange membrane fuel cell	$\omega$	Turbulent eddy frequency ( $s^{-1}$ )
RPM	Revolutions per min ( $r \min^{-1}$ )	$\Gamma_k$	Diffusivity of k
CFD	Computational fluid dynamics	$\Gamma_\omega$	Diffusivity of $\omega$
RSM	Response surface methodology	$G_k$	Production rates of k
CCD	Center composite design	$G_\omega$	Production rates of $\omega$
GA	Genetic algorithm	$Y_k$	Diffusivity of k
Q	Volumetric flow rate	$Y_\omega$	Diffusivity of $\omega$
$Q_m$	Volumetric circulatory flow rate	$D_\omega$	Transverse diffusion term of $\omega$
$r$	External radius of the impeller (mm)	UDF	User-defined function
$r_i$	Inner radius of the impeller (mm)	RTD	Resistance temperature detector
$z$	Number of vanes	SLPM	Standard liter per minute
$\theta$	Angle of the vanes ( $^\circ$ )	DOE	Design of experiments
$h$	Height of the vanes (mm)	X	Independent variable of RSM
$w$	Width of the vanes (mm)	Y	Response variable of RSM
$h_c$	Height of the side channel (mm)	$\eta$	Efficiency
$w_c$	Width of the side channel ( $^\circ$ )	$P_{output}$	Output work (W)
$\theta_s$	Angle of the septum ( $^\circ$ )	$P_{input}$	Input work (W)
Axial clearance	Axial clearance (mm)	V	Volume flow rate ( $m^3 s^{-1}$ )
MRF	Multiple reference frame	$P_{diff}$	Pressure difference (Pa)
$P$	Pressure (kPa)	N	Torque (N m)
$\rho$	Density ( $kg m^{-3}$ )	$\beta$	Regression coefficient of RSM
$R$	Specific gas constant	$\delta$	Error
$T$	Temperature (K)	$\eta_{GA}$	Efficiency calculated by GA
$\vec{u}$	Velocity vector ( $m s^{-1}$ )	$\eta_{CFD}$	Efficiency calculated by CFD
$i, j$ and $k$	Directions	ANOVA	Analysis of variance
$\tau$	Stress tensor	RSME	Root-mean-square error
E	Total energy ( $J kg^{-1}$ )	$S_{gen}$	Total entropy generation rate ( $W m^{-3} K^{-1}$ )
$f$	Mass force (N)	$S_{vis}$	Entropy generation rate of viscous dissipation ( $W m^{-3} K^{-1}$ )
$k_{eff}$	Effective thermal conductivity ( $W m^{-1} K^{-1}$ )	$S_{gen, \bar{D}}$	Entropy generation rate of viscous dissipation average term ( $W m^{-3} K^{-1}$ )
$h_c$	Enthalpy of species $c$ (J)	$S_{gen, D'}$	Entropy generation rate of viscous dissipation pulsation term ( $W m^{-3} K^{-1}$ )
$J_c$	Diffusive flux of species $c$ ( $kg m^{-2} s^{-1}$ )	$\mu$	Dynamic viscosity ( $N s m^{-2}$ )
$Y_c$	Mass fraction of species $c$	$S_{ij}$	Strain rate tensor
SST	Shear stress transport	$S'_{ij}$	Pulsation strain rate tensor
k	Turbulent kinetic energy ( $m^2 s^{-2}$ )		

## References

- Wang, X.; Xu, S.; Xing, C. Numerical and experimental investigation on an ejector designed for an 80 kW polymer electrolyte membrane fuel cell stack. *J. Power Sources* **2019**, *415*, 25–32. [\[CrossRef\]](#)
- Gu, P.; Xing, L.; Wang, Y.; Feng, J.; Peng, X. Transient flow field and performance analysis of a claw pump for FCVs. *Int. J. Hydrogen Energy* **2020**, *46*, 984–997. [\[CrossRef\]](#)
- Seminario-Córdova, R.; Rojas-Ortega, R.J.S. Renewable energy sources and energy production: A bibliometric analysis of the last five years. *Sustainability* **2023**, *15*, 10499. [\[CrossRef\]](#)
- Akinpelu, A.; Alam, M.S.; Shafiullah, M.; Rahman, S.M.; Al-Ismail, F.S.J.S. Greenhouse Gas Emission Dynamics of Saudi Arabia: Potential of Hydrogen Fuel for Emission Footprint Reduction. *Sustainability* **2023**, *15*, 5639. [\[CrossRef\]](#)
- Besagni, G.; Mereu, R.; Inzoli, F.; Chiesa, P. Application of an integrated lumped parameter-CFD approach to evaluate the ejector-driven anode recirculation in a PEM fuel cell system. *Appl. Therm. Eng.* **2017**, *121*, 628–651. [\[CrossRef\]](#)

6. Wang, H.; Ji, C.; Shi, C.; Yang, J.; Wang, S.; Ge, Y.; Chang, K.; Meng, H.; Wang, X. Multi-objective optimization of a hydrogen-fueled Wankel rotary engine based on machine learning and genetic algorithm. *Energy* **2023**, *263*, 125961. [\[CrossRef\]](#)
7. Wang, H.; Ji, C.; Wang, D.; Wang, Z.; Yang, J.; Meng, H.; Shi, C.; Wang, S.; Wang, X.; Ge, Y.; et al. Investigation on the potential of using carbon-free ammonia and hydrogen in small-scaled Wankel rotary engines. *Energy* **2023**, *283*, 129166. [\[CrossRef\]](#)
8. Li, L.; Wang, S.; Zhang, S.; Liu, D.; Ma, S.J.S. The Hydrogen Energy Infrastructure Location Selection Model: A Hybrid Fuzzy Decision-Making Approach. *Sustainability* **2023**, *15*, 10195. [\[CrossRef\]](#)
9. Zhiznin, S.Z.; Vassilev, S.; Gusev, A.L. Economics of secondary renewable energy sources with hydrogen generation. *Int. J. Hydrogen Energy* **2019**, *44*, 11385–11393. [\[CrossRef\]](#)
10. Liu, Y.; Tu, Z.; Chan, S.H. Applications of ejectors in proton exchange membrane fuel cells: A review. *Fuel Process. Technol.* **2021**, *214*, 106683. [\[CrossRef\]](#)
11. Venkatasatish, R.; Chittathuru, D.J.S. Coyote Optimization Algorithm-Based Energy Management Strategy for Fuel Cell Hybrid Power Systems. *Sustainability* **2023**, *15*, 9638. [\[CrossRef\]](#)
12. Azni, M.; Md Khalid, R.; Hasran, U.; Kamarudin, S. Review of the effects of fossil fuels and the need for a hydrogen fuel cell policy in Malaysia. *Sustainability* **2023**, *15*, 4033. [\[CrossRef\]](#)
13. Yin, P.; Chen, J.; He, H.J.S. Control of Oxygen Excess Ratio for a PEMFC Air Supply System by Intelligent PID Methods. *Sustainability* **2023**, *15*, 8500. [\[CrossRef\]](#)
14. Liang, X.; Kang, H.; Shen, J.; Li, Z.; Zeng, R. Review and analysis of hydrogen recirculation devices for compact vehicular proton exchange membrane fuel cells. *J. Power Sources* **2023**, *555*, 232308. [\[CrossRef\]](#)
15. Yin, Y.; Fan, M.; Jiao, K.; Du, Q.; Qin, Y. Numerical investigation of an ejector for anode recirculation in proton exchange membrane fuel cell system. *Energy Convers. Manag.* **2016**, *126*, 1106–1117. [\[CrossRef\]](#)
16. Chen, J.; Siegel, J.B.; Stefanopoulou, A.G.; Waldecker, J.R. Optimization of purge cycle for dead-ended anode fuel cell operation. *Int. J. Hydrogen Energy* **2013**, *38*, 5092–5105. [\[CrossRef\]](#)
17. Hwang, J.-J.; Lin, C.-H.; Kuo, J.-K. Performance analysis of fuel cell thermoelectric cogeneration system with methanol steam reformer. *Int. J. Hydrogen Energy* **2014**, *39*, 14448–14459. [\[CrossRef\]](#)
18. Xiao, Y.; Ye, L.; Yang, Q.X.; Tong, S.Y.; Yin, Y. Hydrogen ejector flow field simulation and performance analysis on PEMFC engine system. *Energy Eng.* **2016**, *6*, 27–33. [\[CrossRef\]](#)
19. Zhang, L.H.; Li, X.J.; Li, J.; Shao, Z.G.; Yi, B.L. Design and performance test of subsonic ejector for proton exchange membrane fuel cell based on thermodynamic model. *Chin. J. Power Sources* **2014**, *38*, 1824–1827.
20. Kim, M.; Sohn, Y.J.; Cho, C.W.; Lee, W.Y.; Kim, C.S. Customized design for the ejector to recirculate a humidified hydrogen fuel in a submarine PEMFC. *J. Power Sources* **2008**, *176*, 529–533. [\[CrossRef\]](#)
21. Zhu, Y.; Li, Y. New theoretical model for convergent nozzle ejector in the proton exchange membrane fuel cell system. *J. Power Sources* **2009**, *191*, 510–519. [\[CrossRef\]](#)
22. Dadvar, M.; Afshari, E. Analysis of design parameters in anodic recirculation system based on ejector technology for PEM fuel cells: A new approach in designing. *Int. J. Hydrogen Energy* **2014**, *39*, 12061–12073. [\[CrossRef\]](#)
23. Brunner, D.A.; Marcks, S.; Bajpai, M.; Prasad, A.K.; Advani, S.G. Design and characterization of an electronically controlled variable flow rate ejector for fuel cell applications. *Int. J. Hydrogen Energy* **2012**, *37*, 4457–4466. [\[CrossRef\]](#)
24. Rao, M.V.; Srisha Jagadeesh, G. Vector Evaluated Particle Swarm Optimization (VEPSO) of Supersonic Ejector for Hydrogen Fuel Cells. *J. Fuel Cell Sci. Technol.* **2010**, *7*, 16–22. [\[CrossRef\]](#)
25. Maghsoodi, A.; Afshari, E.; Ahmadikia, H. Optimization of geometric parameters for design a high-performance ejector in the proton exchange membrane fuel cell system using artificial neural network and genetic algorithm. *Appl. Therm. Eng.* **2014**, *71*, 410–418. [\[CrossRef\]](#)
26. Nikiforow, K.; Koski, P.; Karimaki, H.; Ihonen, J.; Alopaeus, V. Designing a hydrogen gas ejector for 5kW stationary PEMFC system—CFD-modeling and experimental validation. *Int. J. Hydrogen Energy* **2016**, *41*, 14952–14970. [\[CrossRef\]](#)
27. Besagni, G.; Mereu, R.; Chiesa, P.; Inzoli, F. An Integrated Lumped Parameter-CFD approach for off-design ejector performance evaluation. *Energy Convers. Manag.* **2015**, *105*, 697–715. [\[CrossRef\]](#)
28. Pei, P.; Ren, P.; Li, Y.; Wu, Z.; Chen, D.; Huang, S.; Jia, X. Numerical studies on wide-operating-range ejector based on anodic pressure drop characteristics in proton exchange membrane fuel cell system. *Appl. Energy* **2019**, *235*, 729–738. [\[CrossRef\]](#)
29. Yang, Y.; Du, W.; Ma, T.; Lin, W.; Yu, Z. Numerical studies on ejector structure optimization and performance prediction based on a novel pressure drop model for proton exchange membrane fuel cell anode. *Int. J. Hydrogen Energy* **2020**, *45*, 23343–23352. [\[CrossRef\]](#)
30. Yu, M.; Wang, C.; Wang, L.; Wang, X. Flow characteristics of coaxial-nozzle ejector for PEMFC hydrogen recirculation system. *Appl. Therm. Eng.* **2024**, *236*, 121541. [\[CrossRef\]](#)
31. Available online: <https://mp.weixin.qq.com/s/1LcRIEZ8vCdUCeepfElrlg> (accessed on 9 June 2020).
32. Xue, H.; Wang, L.; Zhang, H.; Jia, L.; Ren, J. Design and investigation of multi-nozzle ejector for PEMFC hydrogen recirculation. *Int. J. Hydrogen Energy* **2020**, *45*, 14500–14516. [\[CrossRef\]](#)
33. James, B.D.; Spisak, A.B.; Colella, W.G. Design for Manufacturing and Assembly Cost Estimate Methodology for Transportation Fuel Cell Systems. *J. Manuf. Sci. Eng.* **2014**, *136*, 024503. [\[CrossRef\]](#)
34. Xing, L.; Feng, J.; Chen, W.; Xing, Z.; Peng, X. Development and Testing of a Roots Pump for Hydrogen Recirculation in Fuel Cell System. *Appl. Sci.* **2020**, *10*, 8091. [\[CrossRef\]](#)

35. Hsieh, C.F.; Hwang, Y.W.; Fong, Z.H. Study on the tooth profile for the screw claw-type pump. *Mech. Mach. Theory* **2008**, *43*, 812–828. [CrossRef]
36. Vogelsang, H.; Verhülsdonk, B.; Türk, M.; Hrnig, G. Pulsation problems in rotary lobe pumps. *World Pumps* **1999**, *1999*, 45–46. [CrossRef]
37. Sun, S.K.; Zhao, B.; Jia, X.H.; Peng, X.Y. Three-dimensional numerical simulation and experimental validation of flows in working chambers and inlet/outlet pockets of Roots pump. *Vacuum* **2017**, *137*, 195–204. [CrossRef]
38. Yao, L.; Ye, Z.; Dai, J.S.; Cai, H. Geometric analysis and tooth profiling of a three-lobe helical rotor of the Roots blower. *J. Mater. Process. Technol.* **2005**, *170*, 259–267. [CrossRef]
39. Song, P.; Wang, H.; Zheng, S.; Wei, M.; Zhuge, W.; Zhang, Y. Investigation on the wet compression performance of a co-rotating scroll hydrogen recirculation pump for fuel cell engine systems. *Appl. Therm. Eng.* **2023**, *235*, 121415. [CrossRef]
40. Manfred, D. Hofer Diaphragm Compressors. 2012. Available online: <http://www.andreas-hofer.de/E/downloads/diaphragmcompressor10e02.pdf> (accessed on 16 October 2021).
41. Jia, X.; Chen, J.; Wu, H.; Peng, X. Study on the diaphragm fracture in a diaphragm compressor for a hydrogen refueling station. *Int. J. Hydrogen Energy* **2016**, *41*, 6412–6421. [CrossRef]
42. Hu, Y.; Xu, X.; Wang, W. A new cavity profile for a diaphragm compressor used in hydrogen fueling stations. *Int. J. Hydrogen Energy* **2017**, *42*, 24458–24469. [CrossRef]
43. Zamiri, A.; Lee, B.J.; Chung, J.T. Numerical evaluation of transient flow characteristics in a transonic centrifugal compressor with vaned diffuser. *Aerosp. Sci. Technol.* **2017**, *70*, 244–256. [CrossRef]
44. Wan, Y.; Guan, J.; Xu, S. Improved empirical parameters design method for centrifugal compressor in PEM fuel cell vehicle application. *Int. J. Hydrogen Energy* **2016**, *42*, 5590–5605. [CrossRef]
45. Sun, Z.; Wang, B.; Zheng, X.; Kawakubo, T.; Numakura, R. Effect of bent inlet pipe on the flow instability behavior of centrifugal compressors. *Chin. J. Aeronaut.* **2020**, *33*, 2099–2109. [CrossRef]
46. Martegani, A.D.; Nicolich, M.; Pierdomenico, P. Periphery Compressor Performance; Fluid, Italy, 1990. (In Italian)
47. Hollenberg, J.; Potter, J. An investigation of regenerative blowers and pumps. *J. Manuf. Sci. Eng.* **1979**, *101*, 147–152. [CrossRef]
48. Kim, Y.H.; Kang, S.H. Performance Evaluation of a Regenerative Blower for Hydrogen Recirculation Application in Fuel Cell Vehicles. *Fluids Eng. Div. Summer Meet.* **2006**, *47519*, 311–318. [CrossRef]
49. Badami, M.; Mura, R. Theoretical model with experimental validation of a regenerative blower for hydrogen recirculation in a PEM fuel cell system. *Energy Convers. Manag.* **2010**, *51*, 553–560. [CrossRef]
50. Badami, M.; Mura, M. Leakage effects on the performance characteristics of a regenerative blower for the hydrogen recirculation of a PEM fuel cell. *Energy Convers. Manag.* **2012**, *55*, 20–25. [CrossRef]
51. Badami, M.; Mura, M. Comparison between 3D and 1D simulations of a regenerative blower for fuel cell applications. *Energy Convers. Manag.* **2012**, *55*, 93–100. [CrossRef]
52. Box, G.E.P.; Wilson, K.B. On the Experimental Attainment of Optimum Conditions. *J. R. Stat. Soc. Ser. B* **1951**, *13*, 1–38. [CrossRef]
53. Sung Yang Deok, S.; Soo, H.; Yoon Yong, J. Multi-objective optimization of a Stairmand cyclone separator using response surface methodology and computational fluid dynamics. *Powder Technol.* **2017**, *320*, 51–65. [CrossRef]
54. Singh, D.K.; Tirkey, J.V. Performance optimization through response surface methodology of an integrated coal gasification and CI engine fuelled with diesel and low-grade coal-based producer gas. *Energy* **2022**, *238*, 121982. [CrossRef]
55. Kumar, V.; Jha, K. Multi-objective shape optimization of vortex finders in cyclone separators using response surface methodology and genetic algorithms. *Sep. Purif. Technol.* **2019**, *215*, 25–31. [CrossRef]
56. Arjmandi, H.; Amiri, P.; Pour, M.S. Geometric optimization of a double pipe heat exchanger with combined vortex generator and twisted tape: A CFD and response surface methodology (RSM) study. *Therm. Sci. Eng. Prog.* **2020**, *18*, 100514. [CrossRef]
57. Taghavifar, H.; Jafarmadar, S.; Taghavifar, H.; Navid, A. Application of DoE evaluation to introduce the optimum injection strategy-chamber geometry of diesel engine using surrogate epsilon-SVR. *Appl. Therm. Eng.* **2016**, *106*, 56–66. [CrossRef]
58. Niu, X.; Wang, H.; Hu, S.; Yang, C.; Wang, Y. Multi-objective online optimization of a marine diesel engine using NSGA-II coupled with enhancing trained support vector machine. *Appl. Therm. Eng.* **2018**, *137*, 218–227. [CrossRef]
59. Pfleiderer, C. *Centrifugal Pumps for Fluids and Gas*; Springer: Berlin, Germany, 1955. (In German)
60. ANSYS Fluent Reference Guide; 2021R1. Available online: <https://forum.ansys.com/forums/topic/ansys-fluent-tutorial-guide-2021-r1/> (accessed on 18 February 2024).
61. Nejad, J. Parametric study and performance improvement of regenerative flow pump considering the modification in blade and casing geometry. *Int. J. Numer. Methods Heat Fluid Flow* **2018**, *27*, 1887–1906. [CrossRef]
62. Jang, C.M.; Jeon, H.J. Performance Enhancement of 20kW Regenerative Blower Using Design Parameters. *Int. J. Fluid Mach. Syst.* **2014**, *7*, 86–93. [CrossRef]
63. Nejadrajabali, J.; Riasi, A.; Nourbakhsh, S. Flow pattern analysis and performance improvement of regenerative flow pump using blade geometry modification. *Int. J. Rotating Mach.* **2016**, *2016*, 8628467. [CrossRef]
64. Sreekanth, M.; Sivakumar, R.; Kumar, M.S.S.P.; Karunamurthy, K.; Kumar, M.S.; Harish, R. Regenerative flow pumps, blowers and compressors—A review. *Proc. Inst. Mech. Eng. Part A J. Power Energy* **2021**, *235*, 1992–2013. [CrossRef]
65. Karanth, V.K.; Manjunath, M.S.; Shivakumar Sharma, Y.N. Numerical Study of a Self Priming Regenerative Pump for Improved Performance using Geometric Modifications. *Int. J. Curr. Eng. Technol.* **2015**, *5*, 104–109.

66. Elsayed, K.; Lacor, C. CFD modeling and multi-objective optimization of cyclone geometry using desirability function, artificial neural networks and genetic algorithms. *Appl. Math. Model.* **2013**, *37*, 5680–5704. [[CrossRef](#)]
67. MathWorks, MATLAB R2019b, 2019. Available online: <https://ww2.mathworks.cn/help/matlab/release-notes-R2019b.html> (accessed on 18 February 2024).
68. Kock, F.; Herwig, H. Entropy production calculation for turbulent shear flows and their implementation in cfd codes. *Int. J. Heat Fluid Flow* **2005**, *26*, 672–680. [[CrossRef](#)]

**Disclaimer/Publisher’s Note:** The statements, opinions and data contained in all publications are solely those of the individual author(s) and contributor(s) and not of MDPI and/or the editor(s). MDPI and/or the editor(s) disclaim responsibility for any injury to people or property resulting from any ideas, methods, instructions or products referred to in the content.